# A Genetic Algorithm NURBS-based new approach for fast kinematic limit analysis of masonry vaults

Andrea Chiozzi [a*], Gabriele Milani [b], Antonio Tralli [a]

[a] *Department of Engineering, University of Ferrara,*
*Via Saragat 1, 44122 - Ferrara, Italy*
*E-mail*: *andrea.chiozzi@unife.it, tra@unife.it*

[b] *Department of Architecture, Built Environment and Construction Engineering (A.B.C.),*
*Technical University of Milan, Milan, Italy*
*Piazza Leonardo da Vinci 32, 20133 – Milan, Italy*
*E-mail*: *gabriele.milani@polimi.it*

*(*) Corresponding author.*

*Keywords:* Limit analysis; Masonry; Masonry Vaults; NURBS; Genetic Algorithm

## ABSTRACT

The present paper proposes a new Genetic Algorithm NURBS-based approach for the limit analysis of masonry vaults based on an upper bound formulation. A given masonry vault geometry can be represented by a NURBS (Non-Uniform Rational B-Spline) parametric surface and a NURBS mesh of the given surface can be generated. Each element of the mesh is a NURBS surface itself and can be idealized as a rigid body. An upper bound limit analysis formulation, which takes into account the main characteristics of masonry material is deduced, with internal dissipation allowed exclusively along element edges. The approach is capable of well predicting the load bearing capacity of any masonry vault of generic shape. It is proved that, even by using a mesh constituted by very few elements, a good estimate of the collapse load multiplier is obtained provided that the initial mesh is adjusted by means of a meta-heuristic approach (i.e. a Genetic Algorithm, GA) in order to enforce that element edges accurately represent the actual failure mechanism. The proposed method turns out to be both accurate and much less computationally expensive than existing methods for the limit analysis of masonry vaults.

## 1. INTRODUCTION

Masonry vaults represent one of the most widespread structural typologies in the historical buildings of both Eastern and Western architecture. Therefore, the interest for their preservation is growing over time along with the need for developing new efficient tools to analyze and evaluate their load-bearing capacity. As pointed out in [1,2], modern theory of limit analysis of masonry structures, which has been developed mainly in [3], is a very reliable tool to assess the ultimate load bearing capacity of masonry vaults. According to [3], limit theorems of plasticity, i.e. static (lower bound) theorem and kinematic (upper bound) theorem, can be applied to masonry structures provided that the following conditions are verified: i) the compressive strength of the material is infinite; ii) sliding between parts is prevented; iii) tensile strength of masonry is negligible.

Let us observe that for structures made of clay bricks and mortar, collapse generally occurs at small overall displacements. Moreover, in some cases sliding is possible though with a relatively high friction coefficient [4] and shear failure at the joints can be treated within the framework of non-associate plasticity [5]. Finally, although clay bricks masonry exhibits an almost zero tensile strength and a good compressive strength, the infinite compressive strength hypothesis is questionable and, as shown in [3], it is possible to include finite compressive strength within a limit analysis formulation. Furthermore, material crushing plays a minor role in the collapse behavior of masonry structures, except for very shallow segmental arches, pillars, towers and massive vertical structures.

Other essential aspects concerning actual masonry vaults should be considered, such as the effects due to material heterogeneity, the importance of the overall geometry for achieving the equilibrium, the importance of properly taking into account the infill and the presence of existing cracks [6].

Several computational methods for masonry vaults and arches have been proposed in literature: a number of Finite Element methods (FEM) developed both for nonlinear incremental analysis [7] and for limit analysis [8], the thrust network method [9,10] directly based on a lower bound formulation [11], the Discrete Element Method (DEM) [12–15], the Non-Smooth Contact Dynamics (NSCD) method [16,17] and combined FEM/DEM methods [18,19]. Practical application of these methods requires skilled users and, in the case of thrust network methods, the definition of an equilibrium surface for the vault, which is a priori unknown.

From a technical point of view, the limit analysis FE procedures are mainly based on the upper bound theorem (kinematic approach). For cohesive frictional materials, like masonry, it has been shown that the solution is much more physically sound when dissipation is allowed also on interfaces between adjoining elements and the majority of the models proposed in the recent literature bases on the original idea firstly proposed in [20].

A fundamental issue of limit analysis is that the classical lower and upper bound theorems allow to rigorously bracketing the exact collapse load for a perfectly plastic structure. Therefore, when such theorems are used in combination with the finite element method, the ability to obtain tight bracketing depends not only on the efficient solution of the arising optimization problem, but also on the effectiveness of the elements employed. Classic approaches aimed at improving the performance is to increase the “quality” of velocity (or stress) field interpolation inside elements, for instance using polynomial expansions with degree larger than one [21]. Basing on this idea, for example the so called free Galerkin approach and the p-FEM were used in [22–24].

However, such high order elements pose a particular difficulty when (strict) upper bound analyses must be performed, since the flow rule is required to hold throughout each element, whereas practically it can only be enforced on a finite number of points. To circumvent such a limitation, a constant strain element combined with discontinuities in the displacement field [20] was proposed in the past.

In all those problems, as for instance for masonry vaults, where the complexity of the geometry and the variety of internal stresses acting would require a large number of optimization variables, an alternative possibility of analysis is constituted by the utilization of rigid and infinitely resistant elements with plastic dissipation allowed exclusively on interfaces. This choice is also in agreement with the actual behaviour at failure of masonry, which exhibits collapse mechanisms characterized by large blocks mutually roto-translating.

From a computational standpoint, the number of variables is drastically reduced but unfortunately the failure mechanism is constrained to run exclusively within interfaces, with the consequence of making the problem strongly mesh-dependent with the risk of an incorrect evaluation of the collapse load, which in the framework of the upper bound theorem of limit analysis, is overestimated.

In practice, the alignment of the discontinuities becomes crucial and the FE approach can perform poorly if an unstructured mesh is employed. In order to circumvent this limitation, again re-meshing and adaptive re-meshing strategies could be adopted, see [25,26]. An effective alternative to remeshing has been recently proposed in [27,28] for in-plane problems and masonry vaults respectively. This is an iterative procedure of adaptation of the mesh, where the number of optimization variables is left unaltered at the successive iterations and the nodes belonging to the mesh are moved with a Sequential Linear Programming (SPL) scheme, enforcing some of the interfaces to coincide with the yield lines. It has been proved that the idea is successful and the convergence relatively quick for curved geometries and structures subjected contemporarily to in- and out-of-plane loads, but still needs 50-100 triangular elements for common problems of technical interest and especially requires the evaluation of nodes position first derivatives with respect to analytical expressions of the surfaces where the nodes are located.

NURBS (i.e. Non-Rational Uniform Bi-Spline) are special approximating base functions widely used in the field of 3D modeling [29] for their ability of approximating the actual geometry in an extremely accurate way. Recently, some of the Authors have introduced the idea of using NURBS curves as the basis for the limit analysis of masonry arches through a simple lower bound formulation [30]. In fact, especially when analyzing curved masonry structures, an accurate representation of the original geometry is essential, since a masonry vault can be considered safe (i.e. equilibrium holds) if and only if the thrust surface lies, in every point, within the thickness of the actual vault.

In the present paper, a novel NURBS-based approach for the homogenized limit analysis of masonry vaults based on the upper bound theorem is proposed. Vaults geometry can be described by a NURBS representation of their mid-surface, which can be generated within any commercial free form modeler, together with information about the local thickness at each point of the surface. By exploiting the properties of NURBS functions, a mesh of the given surface, which still provides an exact representation of the vaulted surface, can be obtained. Therefore, a given masonry vault with any geometry can be represented by very few NURBS parametric elements. Each element of the mesh is a NURBS surface itself and is idealized as a rigid body.

Starting from the obtained rigid bodies assembly, an upper bound limit analysis problem with very few optimization variables can be devised, in which dissipation is allowed along element edges only. The main aspects of masonry material (i.e. negligible tensile strength, good compressive strength and orthotropy at failure due to bricks arrangement) are taken into account through homogenization.

Due to the very limited number of rigid elements used, the quality of the collapse load so found depends on the shape and position of the interfaces, where dissipation is allowed. Mesh adjustments are therefore needed, but the utilization of SLP (which would be really cumbersome in presence of curved surfaces, as already pointed out) can be here easily circumvented by adopting a simple meta-heuristic approach of mesh adjustment (like a standard Genetic Algorithm GA or a GA equipped with non standard optimization tools, see [31]).

In the GA-NURBS approach proposed, each individual forming the population is represented by a mesh. For small-to-medium populations (from 5 individuals up to 100), each iteration requires the solution of a Linear Programming problem for each individual. Thanks to the extremely reduced number of NURBS elements used in the discretization (and hence the number of variables of the Linear Programming problem), the computational effort required at each iteration is almost negligible.

After each generation, the GA classically operates on a population of potential failure mechanisms, applying the principle of survival of the fittest to produce better and better approximations to a solution, i.e. moving the interfaces towards the actual failure mechanism. At each generation, a new set of approximations is created by the process of selecting individuals according to their level of fitness (i.e. the value of the collapse load) in the problem domain and breeding them together using operators borrowed from natural genetics (crossover, mutation and reproduction). Authors experienced that this process leads quickly to the evolution of populations of individuals that are better suited to their environment than the individuals that they were created from, with a very accurate estimation of both collapse loads and failure mechanisms after few generation, even in presence of micro GAs. The strength of the proposed GA-NURBS method lies in the fact that even by using a mesh made of very few elements (which therefore require a negligible computational time to have an estimate of collapse loads), it is possible to obtain accurate load multipliers and failure mechanisms, thus exhibiting an edge over existing methods for the collapse analysis of masonry vaults in terms of computational efficiency. Furthermore, since NURBS represent a standard in the field of 3D modeling, the proposed method could easily be integrated within existing commercial CAD software packages, which are popular in the community of professional engineers and architects, thus allowing for the diffusion of safety assessment of masonry vaults through kinematic limit analysis among a broad professional audience.

The paper is organized as follows: in Section 2 a synthetic survey is given about how the geometric shape of a masonry vault can be described by a NURBS surface representation and a NURBS mesh can be defined on it. In Section 3, the upper bound limit analysis formulation with NURBS rigid elements and interfaces is proposed, based on the NURBS geometric representation of the masonry vault, which allows to compute the collapse load for a set of given failure mechanisms. Here a brief review of the homogenization approach used to estimate homogenized failure surfaces on curved interfaces is also provided. Section 4 outlines the Genetic Algorithm strategy, which is capable of selecting the correct failure mechanism, by adequately adjusting the initial mesh. Finally, Section 5 is devoted to validate the proposed procedure by a number of numerical simulation on real structural examples.

## 2. NURBS GEOMETRIC DESCRIPTION

Description and computation of geometries in commercial CAD packages are based on B-Splines and NURBS approximating functions. More precisely, NURBS basis functions are built on B-splines basis functions, which are piecewise polynomial functions defined by a sequence of coordinates $\Xi = \{\xi_1, \xi_2, ..., \xi_{n+p+1}\}$, also known as the knot vector, where the so-called knots, $\xi_i \in [0,1]$, are points in a parametric domain, in which $p$ and $n$ denote the polynomial order and the total number of basis functions, respectively. Once the order of the basis function and the knot vector are known, the $i$-th B-spline basis function, $N_{i,p}$, can be computed by means of the Cox-de Boor recursion formula [29], which is not reported here for the sake of brevity.

As previously mentioned, B-splines are the starting point for the computation of the NURBS basis functions. Indeed, given a set of weights, $w_i \in \mathbb{R}$, the NURBS basis functions, $R_{i,p}$, read

$$R_{i,p}(\xi) = \frac{N_{i,p}(\xi) w_i}{\sum_{i=1}^{n} N_{i,p}(\xi) w_i}. \tag{1}$$

NURBS share many properties with B-spline basis functions. Among these, they are all nonnegative, they have a compact support, and build a partition of unity (PoU), that is

$$\sum_{i=1}^{n} N_{i,p}(\xi) = \sum_{i=1}^{n} R_{i,p}(\xi) = 1 \tag{2}$$

for each $\xi \in [0,1]$ [32]. Hence, according to Eqs. (1) and (2) B-spline basis functions can be thought of as NURBS basis functions when all weights $w_i$ are equal to one. However, NURBS basis functions have the great advantage of representing exactly the geometry of a wide set of curves such as circles, ellipses, and parabolas [32], and of the surfaces that can be generated by these curves. Geometries that can be generated with B-spline and NURBS are obtained as linear combinations of basis functions [32]. If one considers a set of NURBS basis functions $R_{i,p}$, a NURBS curve of degree $p$ is a parametric curve in the three-dimensional Euclidean space defined as

$$\mathbf{C}(u) = \sum_{i=1}^{n} R_{i,p}(\xi) \mathbf{B}_i \tag{3}$$

where coefficients $\mathbf{B}_i \in \mathbb{R}^3$ are known as control points. Unlike standard Lagrange and Hermite approximations, NURBS geometries do not usually interpolate these points. The continuity of the curve follows from that of the adopted basis functions, which is generally $C^{p-1}$ throughout the domain. However, if a knot has multiplicity, *m*, the continuity decreases *m* times at that point [32]. Analogously, a NURBS surface of degree *p* in the *u*-direction and *q* in the *v*-direction is a parametric surface in the three-dimensional Euclidean space defined as

$$\mathbf{S}(u,v) = \sum_{i=0}^{n}\sum_{j=0}^{m} R_{i,j}(u,v)\mathbf{B}_{i,j} \tag{4}$$

where $\{\mathbf{B}_{ij}\}$ form a bidirectional net of control points. A set of weights $\{w_{i,j}\}$ and two separate knot vectors in both *u* and *v* directions must be defined. Given a NURBS surface $\mathbf{S}(u,v)$, isoparametric curves on the surface can be defined by fixing one parameter in the parameter space and letting the other vary. By fixing $u = u_0$ the isoparametric curve $\mathbf{S}(u_0, v)$ is defined on the surface $\mathbf{S}$, whereas by fixing $v = v_0$ the isoparametric curve $\mathbf{S}(u, v_0)$ is obtained. Many commercial free form surface modelers, such as Rhinoceros® [33], utilize NURBS representation and its properties to generate and manipulate surfaces in the three-dimensional space. In what follows, simple vault geometries have been generated within Rhinoceros and the resulting NURBS structure has been imported within a MATLAB® environment through the IGES (Initial Graphics Exchange Specification) standard [34]. Once the NURBS structure has been transferred to the MATLAB® environment, it is possible to manipulate it by exploiting NURBS properties in order to define a NURBS mesh on the given surface, i.e. a mesh in which each element is a NURBS surface itself. When working with simple surfaces like the one considered in the present contribution, the easiest way to generate a NURBS mesh on the given surface is to define a subdivision of the two-dimensional parameters space *u*-*v*, which follows from subdividing the knot vectors in both *u* and *v* directions into equal intervals. The resulting mesh is defined by isoparametric curves on the surface in the three-dimensional Euclidean space.

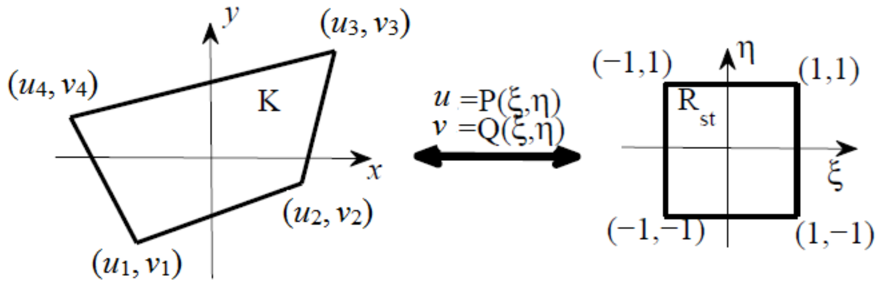


**Fig. 1** Linear mapping between $K$ and $R_{st}$.

Each element of the mesh is a NURBS surface and its edges are branches of isoparametric curves belonging to the initial surface. More precisely, the counter-image of each element of the mesh is a rectangle $S_{ij} = [u_i, u_{i+1}] \times [v_j, v_{j+1}] \in \mathbb{R}^2$ defined in the parameters space.

More in general, different meshes of the NURBS surface can be obtained for arbitrary partitions of the parameters space into quadrilateral or triangular domains. The image of each domain is an element of the mesh, which is a NURBS surface itself. The union of all elements of the chosen mesh is equal to the original surface, no matter how coarse the mesh is. For each element of the mesh, $E_i$, be the domain $K_i$ its counter-image in the two-dimensional parameters space *u*-*v*.

Therefore, the area of the surface can be computed through the following relation:

$$A_i = \iint_{E_i} dS = \iint_{K_i} \left\| \mathbf{S}_u \times \mathbf{S}_v \right\| du\, dv \qquad (5)$$

where $\mathbf{S}_u$ and $\mathbf{S}_v$ are partial derivatives of the parametric surface $\mathbf{S}(u,v)$ in the $u$ and $v$ directions. Analogously, the center of mass of each element may be computed with the following relation:

$$\mathbf{c} = \frac{1}{A_i} \iint_{E_i} \mathbf{x}\, dS = \iint_{K_i} \mathbf{S}(u,v) \left\| \mathbf{S}_u \times \mathbf{S}_v \right\| du\, dv \qquad (6)$$

Since integrals (5) and (6) are evaluated on general quadrangular domains, an isoparametric approach can be adopted for their numerical computation. Let $K$ be a quadrilateral domain in the parameters space with straight boundary lines and vertices $(u_i, v_i)$, $i = 1,2,3,4$ arranged in counter-clockwise order (Fig. 1). The idea is simple: first transform the quadrilateral domain $K$ to the standard quadrilateral element $R_{st}$ and then apply the Gaussian quadrature. The transformation can be done by using the following nodal shape functions for quadrilaterals:

$$\begin{aligned} N_1(\xi,\eta) &= \frac{1}{4}(1-\xi)(1-\eta), \\ N_2(\xi,\eta) &= \frac{1}{4}(1+\xi)(1-\eta), \\ N_3(\xi,\eta) &= \frac{1}{4}(1+\xi)(1+\eta), \\ N_4(\xi,\eta) &= \frac{1}{4}(1-\xi)(1+\eta), \end{aligned} \tag{7}$$

Note that $N_i(\xi,\eta)=1$ at node $i$, and zero at other nodes. Now, it is necessary to construct a linear mapping to map the quadrilateral domain $K$ to the standard square $R_{st}=[-1,\ 1]\times[-1,\ 1]$ in the auxiliary two-dimensional space $(\xi,\eta)$ (Fig. 1). The mapping can be achieved conveniently by using the nodal shape function as follows:

$$\begin{aligned} u &= P(\xi,\eta) = \sum_{i=1}^{4} u_i N_i(\xi,\eta) \\ v &= Q(\xi,\eta) = \sum_{i=1}^{4} v_i N_i(\xi,\eta) \end{aligned} \tag{8}$$

Then, a given integral over $K$ can be rewritten in the following way as an integral over $R_{st}$:

$$\iint_K F(u,v)\,du\,dv = \iint_{R_{st}} F(P(\xi,\eta),\ \mathrm{Q}(\xi,\eta))\left|J(\xi,\eta)\right| d\xi\,d\eta, \tag{9}$$

where $J(\xi,\eta)$ is the Jacobian of the transformation (8).

Therefore, it is now possible to apply the Gaussian quadrature rule for standard square domains:

$$\iint_K F(u,v)\,du\,dv = \sum_{i=1}^{N}\sum_{j=1}^{N} w_i w_j F(P(\xi_i,\eta_j),\mathrm{Q}(\xi_i,\eta_j))\left|J(\xi_i,\eta_j)\right|. \tag{10}$$

where $(\xi_i,\eta_j)$ and $w_j$ are Gaussian quadrature points and weights respectively.

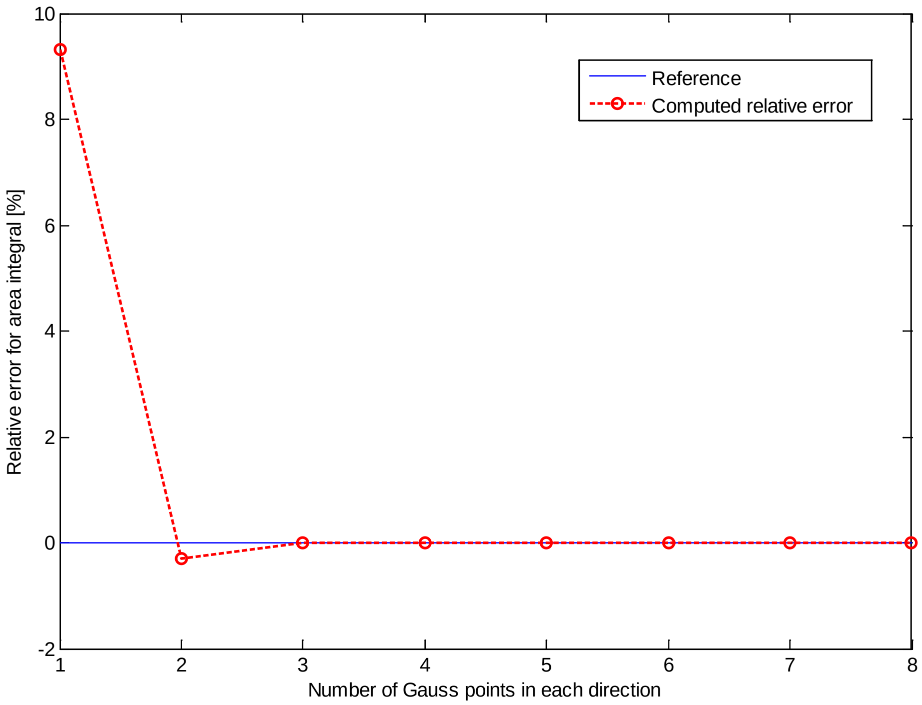


**Fig. 2** Numerical integration convergence graph with increasing Gauss points number.

In the numerical examples shown in Section 5, a 3-points in each direction Gauss rule has been adopted for computing area (5) and center of mass (6) integrals, since this choice provides the needed accuracy. Fig. 2 reports how fast numerical evaluated area integrals (5) converge to the exact value by increasing the number of Gauss points in each direction. In fact a 3-points per direction Gauss rule is proven to be sufficiently accurate for our scope. Finally, two more definition are needed in order to apply limit analysis to the obtained assembly of NURBS elements. Given that the NURBS surface $\mathbf{S}(u,v)$ has, in each point, a regular parametrization, i.e. partial derivative vectors $\mathbf{S}_u$ and $\mathbf{S}_v$ are linearly independent for each couple of parameters ($u$, $v$), the *tangent plane* is the affine plane in $\mathbb{R}^3$ spanned by these vectors and passing through the point $\mathbf{S}(u,v)$.

Any *tangent vector* can be uniquely decomposed into a linear combination of $\mathbf{S}_u$ and $\mathbf{S}_v$. The cross product of these vectors is a normal vector to the tangent plane. Dividing this vector by its length yields a *unit normal vector* to the parametrized surface at a point ($u$, $v$):

$$\mathbf{n}(u,v) = \frac{\mathbf{S}_u(u,v) \times \mathbf{S}_v(u,v)}{\left\| \mathbf{S}_u(u,v) \times \mathbf{S}_v(u,v) \right\|} \tag{11}$$

## 3. KINEMATIC LIMIT ANALYSIS

Limit analysis is a powerful tool to assess the structural safety level of a masonry construction. As already discussed, given the NURBS geometric representation of the vaulted surface, a NURBS mesh can be defined on the same surface. Each element of the mesh, which is a NURBS surface itself, can be regarded as a rigid body. Starting from the geometrical properties of each element, an upper bound formulation can be outlined and implemented through a linear programming algorithm in order to assess the ultimate load bearing capacity of a given masonry vault. This paragraph summarizes the proposed upper bound formulation. Be $N_E$ the number of elements composing the NURBS mesh, which geometrically represents the vaulted surface. Each element is considered as a rigid element. Thus, the kinematics of each element is determined by the six (three translational and three rotational) generalized velocity components $\{u_x^i, u_y^i, u_z^i, \Phi_x^i, \Phi_y^i, \Phi_z^i\}$ of its center of mass $G_i$, expressed in a global reference system $Oxyz$. On the structure, dead loads $\mathbf{F}_0$ and live loads $\mathbf{\Gamma}$ are acting. Internal dissipation is assumed to occur only along element interfaces. Indicating by $N_I$ the number of interfaces, total internal dissipation power $D_{\text{int}}$ is equal to the sum of the power dissipated along each interface $P_{\text{int}}^i$. Furthermore, total internal dissipation power $D_{\text{int}}$ is equal to the sum of the powers of live ($\mathbf{1} \cdot \Gamma$) and dead ($\mathbf{F_0}$) loads, indicated as $P_{\mathbf{\Gamma}}$ and $P_{\mathbf{F_0}}$ respectively:

$$D_{\text{int}} = \sum_{i=1}^{N_I} P_{\text{int}}^i = P_{\mathbf{\Gamma}} + P_{\mathbf{F_0}} \tag{12}$$

$\Gamma$ is a load multiplier. The linear programming problem related to the kinematic formulation of limit analysis consists in an appropriate minimization of the load multiplier $\Gamma$ under the action of suitable constraints, which are described in the following Subsections. The vector of unknowns of the linear programming problem, $\mathbf{X}$, contains the six generalized velocity components for each element and a number of plastic multipliers along each interface which will be defined in Subsection 3.2.

### *3.1 Geometric constraints*

Vertex belonging to element free edges, which do not constitute an element interface, can be subjected to external kinematic constraints, by imposing an assigned value for translational and/or rotational velocities at these points. For each of such vertex $V_j$, kinematic constraints can be expressed in terms of generalized velocities of the center of mass of the *i*-th element they belong to. For example, in case only translational velocities of a given vertex $V_j$, belonging to element *i*, are constrained to zero, the following relation holds as a geometric constraint:

$$\mathbf{u}_{V_j} = \mathbf{u}^i + \mathbf{R}\left[\mathbf{x}_{V_j} - \mathbf{x}_{G_i}\right] = \mathbf{0} \tag{13}$$

where $\mathbf{u}_{V_j} = [u_x^{V_j}, u_y^{V_j}, u_z^{V_j}]^T$ are the three translational velocity components of the vertex $V_j$, $\mathbf{u}^i = [u_x^i, u_y^i, u_z^i]^T$ are the three (unknown) translational velocity components of the center of mass of element *i* to whom vertex $V_j$ belongs, and $\mathbf{R}$ is the rotation matrix:

$$\mathbf{R} = \begin{bmatrix} 0 & -\Phi_z^i & \Phi_y^i \\ \Phi_z^i & 0 & -\Phi_x^i \\ -\Phi_y^i & \Phi_x^i & 0 \end{bmatrix}, \tag{14}$$

whose elements are the (unknown) generalized rotational velocities of the center of mass of element *i*. In general, all linear geometric constraints can be re-written in the following standard form:

$$\mathbf{A}_{eq,geom}\mathbf{X} = \mathbf{b}_{eq,geom} \tag{15}$$

where $\mathbf{A}_{eq,geom}$ is the matrix of geometric constraints and $\mathbf{b}_{eq,geom}$ the corresponding vector of coefficients.

## *3.2 Compatibility constraints*

Up to now, the thickness of the vaulted surface was not discussed. In fact, interfaces between elements are planar surfaces whose height in each point of their midline corresponds to the local thickness of the vault. In order to enforce plastic compatibility along interfaces and correctly evaluate dissipation power, intrados and extrados edges of each interface have been subdivided into an assigned number $(N_{sd}+1)$ of points $P_i$ (see Fig. 3).

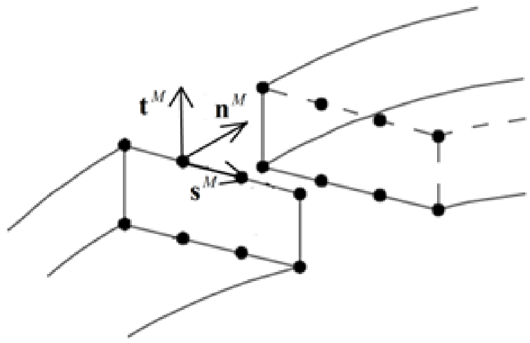


**Fig. 3**. Masonry-masonry interface and corresponding local reference system.

On each point $P_i$, a local reference system $(\mathbf{n}, \mathbf{s}, \mathbf{t})$ has been defined, where $\mathbf{n}$ is the unit vector normal to the interface, $\mathbf{s}$ is the tangential unit vector in the longitudinal direction and $\mathbf{t}$ is the tangential unit vector in the transversal direction. On each point $P_i$ of each interface, which separates the two elements $E'$ and $E''$, the following compatibility equation must hold:

$$\Delta\tilde{\mathbf{u}} = \dot{\boldsymbol{\lambda}} \frac{\partial f}{\partial \boldsymbol{\sigma}} \tag{16}$$

where $\boldsymbol{\sigma} = [\sigma_{nn}, \sigma_{ns}, \sigma_{nt}]$ is the stress vector acting on $P_i$ in the three local reference directions, $f(\boldsymbol{\sigma})$ is a suitable yield function and $\dot{\boldsymbol{\lambda}}$ is an unknown plastic multiplier vector. In Eq. (16), $\Delta\tilde{\mathbf{u}}$ is the representation in the local reference system of the quantity $\Delta\mathbf{u}$ in the global reference system which is defined as:

$$\Delta\mathbf{u} = \mathbf{u}'_{P_i} - \mathbf{u}''_{P_i} \tag{17}$$

where $\mathbf{u}'_{P_i}$ and $\mathbf{u}''_{P_i}$ are the vectors composed of three translational velocity components of the point $P_i$, seen as belonging to elements $E'$ and $E''$ respectively. $\Delta\mathbf{u}$ is related to $\Delta\tilde{\mathbf{u}}$ through the following relation:

$$\Delta\tilde{\mathbf{u}} = \tilde{\mathbf{R}}\Delta\mathbf{u} \tag{18}$$

where $\tilde{\mathbf{R}}$ is a suitable $3\times3$ rotation matrix whose rows are respectively the components of the three local vectors $(\mathbf{n}, \mathbf{s}, \mathbf{t})$ expressed in the global reference system.

The yield surface $f(\boldsymbol{\sigma})$ has been obtained by means of a homogenization procedure based on the so-called Method of Cells (MoC). Such approach was originally proposed in [35] for unidirectional composites reinforced by a regular pattern of long, reinforcing fibers. MoC has been recently extended to masonry in [36] for the macroscopic elastic and creep coefficients determination in closed form and in [37] for the limit analysis case. The method, applied to running bond masonry in-plane loaded, consists into the subdivision of the REV into 6 rectangular sub-cells, as shown in Fig. 4, where the velocity field is approximated using two sets of strain-rate periodic piecewise differentiable velocity fields, one for normal and one for shear deformation mode. Let us indicate with the symbols $u_1^{n(i)}$ and $u_2^{n(i)}$ vertical and horizontal velocity fields of the $i$-th cell for deformation mode acting axially along vertical and horizontal directions. Assuming the same periodic field proposed for displacements in the elastic range in [36], the following relations hold:

$$
\begin{aligned}
& u_1^{n(2)} = 2U_1 \frac{x_1}{b_b} \quad u_2^{n(1)} = -2W_1 \frac{x_2}{h_b} \\
& u_1^{n(2)} = U_1 + \frac{\left(U_2 - U_1\right)\left(x_1 - \frac{b_b}{2}\right)}{b_m} \qquad u_2^{n(2)} = -2\frac{x_2}{h_b}\left(\frac{2\left(W_1 - W_2\right)\left|\frac{b_m + b_b}{2} - x_1\right|}{b_m} + W_2\right) \\
& u_1^{n(3)} = u_1^{n(1)} - \frac{\left(U_1\left(1 + 2\alpha_b\right) - U_2\right)\left(\frac{h_b}{2} - x_2\right)}{2h_m} \quad u_2^{n(3)} = -W_1 + \frac{\left(W_1 - W_3\right)\left(x_2 - \frac{h_b}{2}\right)}{h_m} \\
& u_1^{n(4)} = u_1^{n(1)} + \frac{\left(U_1\left(1 + 2\alpha_b\right) - U_2\right)\left(\frac{h_b}{2} - x_2\right)}{2h_m} \quad u_2^{n(4)} = u_2^{n(3)} \\
& u_1^{n(5)} = U_1 - \frac{\left(U_1\left(1 + 2\alpha_b\right) - U_2\right)\left(\frac{b_b + b_m}{2} - x_1\right)\left(x_2 - \frac{h_b}{2}\right)}{b_m h_m} - \frac{\left(U_1 - U_2\right)\left(x_1 - \frac{b_b}{2}\right)}{b_m} \\
& u_2^{n(5)} = -W_3 \frac{x_2 - \frac{h_b}{2}}{h_m} - 2\frac{\left(W_2 \frac{b_m}{2} - \left(W_2 - W_1\right)\left|\frac{b_b + b_m}{2} - x_1\right|\right)\left(\frac{h_b}{2} + h_m - x_2\right)}{b_m h_m} \\
& u_1^{n(6)} = 2\frac{x_1}{b_b}\left(U_1 - \frac{\left(U_1 + \frac{U_1 - U_2}{2\alpha_b}\right)\left(x_2 - \frac{h_b}{2}\right)}{h_m}\right) \\
& u_2^{n(6)} = -W_1 + \frac{\left(W_2 - W_3 + 2\left(W_1 - W_2\right)\frac{\left|x_1\right|}{b_m}\right)\left(x_2 - \frac{h_b}{2}\right)}{h_m}
\end{aligned}
\tag{19}
$$

An additional constraint $W_1 = W_2$ is imposed in the model in order to avoid bilinear terms of the velocity field in cross-joints. Bi-linearity makes the check of the associated flow rule inside cross-joints cumbersome, with an experienced negligible modification of the final result. Frame of reference $x_1$-$x_2$ and geometrical meaning of the symbols are provided in Fig. 4(a): $h_b$ is the brick height, $h_m$ is the thickness of the bed joints, $\alpha_b$ is the ratio between $b_m$ and $b_b$, respectively bed joint thickness and brick length. Fields (19) depend on the four degrees of freedom $U_1$, $U_2$, $W_1$, $W_2 = W_1$ and $W_3$ with clear physical meaning represented in Fig. 4(b) and Fig. 5.

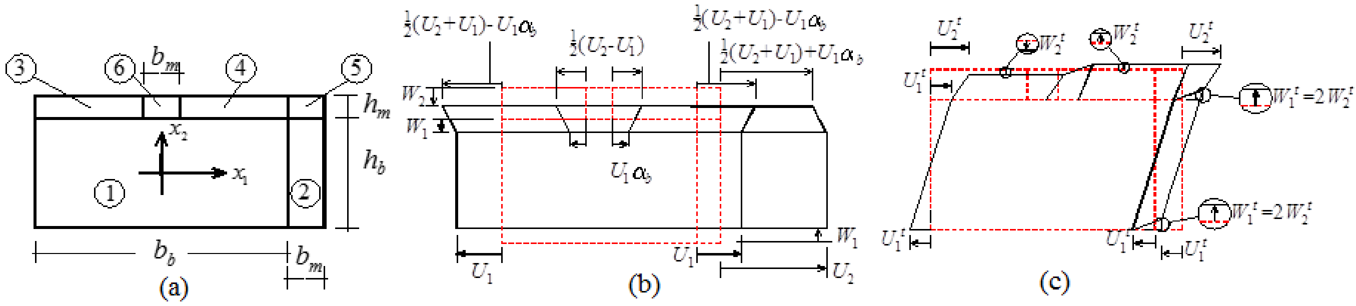


**Fig. 4:** (a) REV adopted in the MoC approach and subdivision into cells; (b) Strain-periodic kinematically admissible velocity field under horizontal or vertical macroscopic normal stresses; (c) Strain-periodic kinematically admissible velocity field under macroscopic shear stress.

It is interesting to notice that velocity fields inside each cell are either linear (cells 1, 3, 4) or quadratic (cells 2, 5, 6). When a shear deformation mode is applied on the REV, the following fields of velocity are assumed inside each cell:

$$
\begin{aligned}
& u_1^{t(1)} = 2U_1^t \frac{x_2}{h_b} \quad u_2^{t(1)} = 0 \quad u_1^{t(2)} = u_1^{t(1)} \quad u_2^{t(2)} = W_1^t \frac{x_1 - \frac{b_b}{2}}{b_m} \\
& u_1^{t(3)} = U_1^t + \frac{U_2^t - U_1^t}{h_m}\left(x_3 - \frac{h_b}{2}\right) \quad u_2^{t(3)} = -W_2^t \frac{x_2 - \frac{h_b}{2}}{h_m} \\
& u_1^{t(4)} = u_1^{t(3)} \quad u_2^{t(4)} = -u_2^{t(3)} \\
& u_1^{t(5)} = u_1^{t(3)} \quad u_2^{t(5)} = -W_1^t \frac{\left(x_1 - \frac{b_b + b_m}{2}\right)\left(x_2 - \frac{h_b}{2}\right) - h_m\left(x_1 - \frac{b_b}{2}\right)}{b_m h_m} \\
& u_1^{t(6)} = u_1^{t(3)} \quad u_2^{t(6)} = W_1^t \frac{x_1\left(x_2 - \frac{h_b}{2}\right)}{b_m h_m}
\end{aligned}
\tag{20}
$$

Symbols $u_1^{t(i)}$ and $u_2^{t(i)}$ in equation (20) indicate vertical and horizontal velocity fields of the i-th cell for the shear deformation mode imposed. In equation (20) independent variables (DOFs) are represented by $U_1^t$, $U_2^t$, $W_1^t$ and $W_2^t$, whose physical meaning is depicted in Fig. 4(c) and Fig. 6.

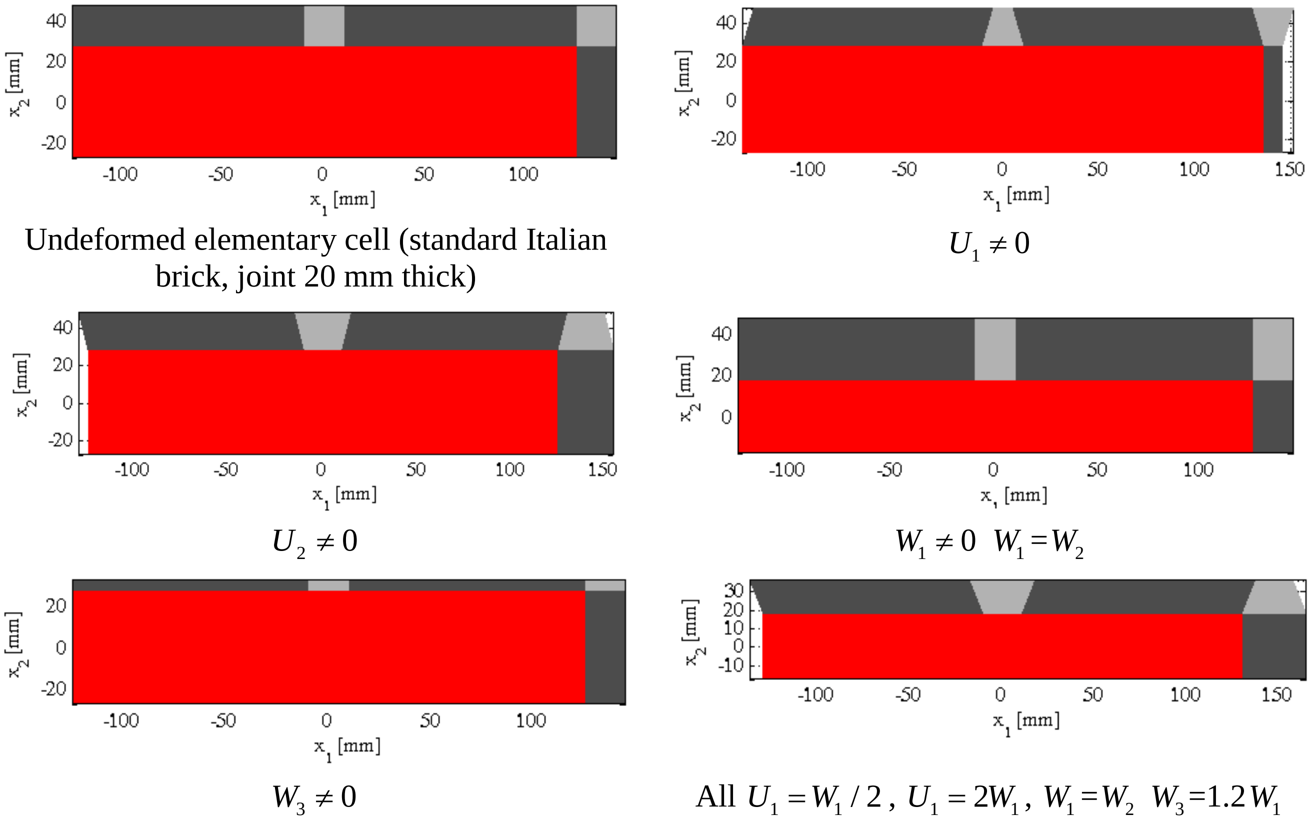


**Fig. 5:** Strain-rate periodic kinematically admissible velocity field under horizontal or vertical macroscopic stresses.

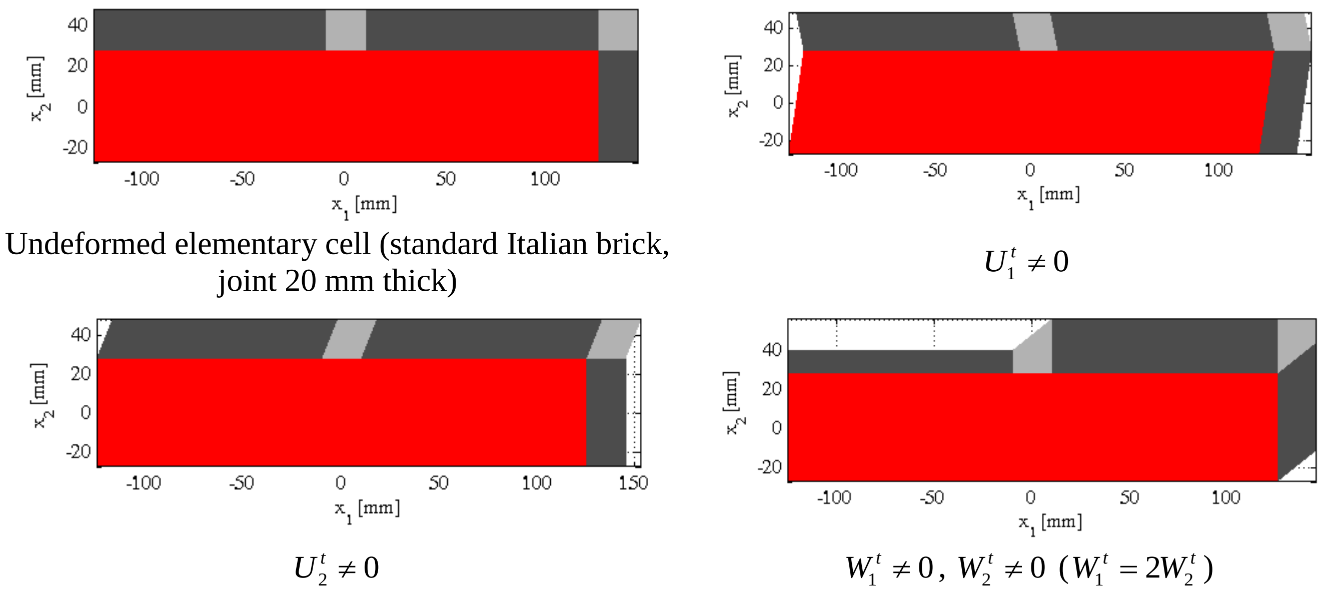


**Fig. 6:** Strain-rate periodic kinematically admissible velocity field under shear.

An additional constraint $W_1^t = 2W_2^t$ is imposed in the model to make the velocity field compatible between cross-joints and contiguous sub-cells. According to the kinematic theorem of limit analysis and assuming the velocity field over the RVE to be approximated by means of the expressions provided by equations (19)-(20) the associativity of the plastic flow over each sub-cell must be prescribed. Let $u_1 = u_1^{n(i)} + u_1^{t(i)}$ and $u_2 = u_2^{n(i)} + u_2^{t(i)}$ denote the horizontal and vertical components of the velocity field in the ($i$)-th sub-cell. At each point of any sub-cell, the associated flow rule translates into three equality constrains, which can be written as $\dot{\boldsymbol{\varepsilon}}_{pl}^{(i)} = \begin{bmatrix} \frac{\partial v_1}{\partial y_1} & \frac{\partial v_2}{\partial y_2} & \frac{\partial v_1}{\partial y_2} + \frac{\partial v_2}{\partial y_1} \end{bmatrix} = \dot{\lambda}^{(i)} \frac{\partial \mathbf{f}_{b,m}}{\partial \boldsymbol{\sigma}}$, where $\dot{\boldsymbol{\varepsilon}}_{pl}^{(i)}$ is the plastic strain rate field in the ($i$)-th sub-cell, $\dot{\lambda}^{(i)}$ ($\geq 0$) is the rate of the plastic multiplier, and $\mathbf{f}^{b,m}$ is the (non) linear failure surface of either bricks ($b$) or mortar ($m$).

Let the failure surfaces of bricks and mortar be approximated by $m$ planes, so that each strength criterion is defined by a set of linear inequalities of the form $\mathbf{f}_{b,m} \equiv \mathbf{A}^{in}\boldsymbol{\sigma} \leq \mathbf{b}^{in}$. As $\dot{\boldsymbol{\varepsilon}}_{pl}^{(i)}$ varies at most linearly within each sub-cell, plastic admissibility is checked only at three of the corners. Hence, nine linear equality constraints per sub-cell are introduced in matrix form as $\mathbf{A}_{U(i)}^{eq}\mathbf{U} + \mathbf{A}_{\lambda(i)}^{eq}\dot{\boldsymbol{\lambda}}^{(i)} = \mathbf{0}$, where $\mathbf{U}$ is an array collecting the 7 DOFs describing the microscopic velocity field (i.e. $\mathbf{U} = \{U_1, U_2, W_1, W_2, U_1^t, U_2^t\ W_1^t\}^T$), $\dot{\boldsymbol{\lambda}}^{(i)} = \begin{bmatrix} \dot{\boldsymbol{\lambda}}_A^{(i)T} & \dot{\boldsymbol{\lambda}}_B^{(i)T} & \dot{\boldsymbol{\lambda}}_C^{(i)T} \end{bmatrix}^T$ is an array of 3$m$ entries, collecting the rates of the plastic multipliers $\dot{\boldsymbol{\lambda}}_J^{(i)}$ at three of the corners of the rectangular sub-cell ($J$ = $A$, $B$, $C$), and $\mathbf{A}_{U(i)}^{eq}$, $\mathbf{A}_{\lambda(i)}^{eq}$ are a 9×7 and a 9×3$m$ matrix, respectively. The plastic admissibility conditions are then assembled cell by cell into the following global system of equality constraints:

$$\mathbf{A}_U^{eq}\mathbf{U} + \mathbf{A}_\lambda^{eq}\dot{\boldsymbol{\lambda}} = \mathbf{0} \qquad (21)$$

where $\mathbf{A}_U^{eq} = \begin{bmatrix} \mathbf{A}_{U(1)}^{eq\ T} & \ldots & \mathbf{A}_{U(6)}^{eq\ T} \end{bmatrix}^T$, $\dot{\boldsymbol{\lambda}} = \begin{bmatrix} \dot{\boldsymbol{\lambda}}^{(1)T} & \ldots & \dot{\boldsymbol{\lambda}}^{(6)T} \end{bmatrix}^T$, and $\mathbf{A}_\lambda^{eq}$ is a block matrix of dimension (6·9)×(6·3$m$), which can be expressed as:

$$\mathbf{A}_{\lambda}^{eq} = \mathbf{A}_{\lambda(1)}^{eq} \oplus \mathbf{A}_{\lambda(2)}^{eq} \oplus \cdots \oplus \mathbf{A}_{\lambda(6)}^{eq} \tag{22}$$

where $\oplus$ denotes direct sum. Let $B$ and $C$ be a couple of corners at the opposite ends of one of the diagonals of the ($i$)-th rectangular sub-cell. The internal power dissipated within the sub-cell can be written as:

$$\pi_{in}^{(i)} = \frac{\Omega^{(i)}}{2}\left(\mathbf{b}_{in}^{(i)T}\dot{\boldsymbol{\lambda}}_{B}^{(i)} + \mathbf{b}_{in}^{(i)T}\dot{\boldsymbol{\lambda}}_{C}^{(i)}\right) = \frac{\Omega^{(i)}}{2}\begin{bmatrix}\mathbf{0}_{1\times m} & \mathbf{b}_{in}^{(i)T} & \mathbf{b}_{in}^{(i)T}\end{bmatrix}\dot{\boldsymbol{\lambda}}^{(i)}, \tag{23}$$

where $\mathbf{0}_{1\times m}$ is an array of $m$ zero entries and $\Omega^{(i)}$ is the area of the ($i$)-th sub-cell. The power dissipated inside the whole RVE is obviously the sum of the contributions of each sub-cell, i.e.:

$$\pi_{in} = \sum_{i=1}^{6}\frac{\Omega^{(i)}}{2}\begin{bmatrix}\mathbf{0}_{1\times m} & \mathbf{b}_{in}^{(i)T} & \mathbf{b}_{in}^{(i)T}\end{bmatrix}\dot{\boldsymbol{\lambda}}^{(i)}. \tag{24}$$

The array of the macroscopic stress components can be expressed as $\boldsymbol{\Sigma} = \Lambda\begin{bmatrix}\alpha & \beta & \gamma\end{bmatrix}^{T}$, where $\Lambda$ is the load multiplier and $\alpha$, $\beta$, $\gamma$ are the director cosines of the direction of $\boldsymbol{\Sigma}$ in the space of the homogenized in-plane stresses. The power of the external loads is simply $\pi_{ex} = \Lambda\begin{bmatrix}\alpha & \beta & \gamma\end{bmatrix}\mathbf{D}$ with normalization condition given by $\begin{bmatrix}\alpha & \beta & \gamma\end{bmatrix}\mathbf{D} = 1$. Any point of the homogenized failure surface is thus determined solving the following constrained minimization problem:

$$\min \pi_{\text{in}} \left\{ \text{subject to} \begin{cases} \begin{bmatrix}\alpha & \beta & \gamma\end{bmatrix}\mathbf{D} = 1 & \text{(a)} \\ \mathbf{A}_{U}^{eq}\mathbf{U} + \mathbf{A}_{\lambda}^{eq}\dot{\boldsymbol{\lambda}} = \mathbf{0} & \text{(b)} \\ \mathbf{D} = \dfrac{1}{A}\displaystyle\int_{\partial Y} \mathbf{v} \overset{s}{\otimes} \mathbf{n}\, dS & \text{(c)} \\ \dot{\boldsymbol{\lambda}} \geq \mathbf{0} & \text{(d)} \end{cases} \right. \tag{25}$$

where (a) is the normalization condition, (b) is the set of equations representing the admissibility of the plastic flow, Eq.(21), and (c) links the homogenized strain rate with the local velocity field.

It is interesting to note that the independent variables entering into the optimization problem (25) are the three components of the macroscopic strain rate $\boldsymbol{D}$, the 6×3$m$ plastic multipliers $\dot{\boldsymbol{\lambda}}$ and the 7 DOFs defining the microscopic velocity field. Via the normalization condition and equating the internal power dissipation to the power of the external loads, it can be easily shown that $\Lambda = \min\ \pi_{in}$.

With the iterative solution of equation (25) it is possible to easily provide a linearization for $f(\boldsymbol{\sigma})$ the assigned yield surface. Let us indicate with the equation $A_i\sigma_{nn} + B_i\sigma_{ns} + C_i\sigma_{nt} = 1$ the i-th plane representing $f(\boldsymbol{\sigma})$. In such a way Eq. (16) simplifies to the equation:

$$\Delta\tilde{\mathbf{u}} = \begin{bmatrix} \sum_{i=1}^{N^{pl}} A_i\dot{\lambda}^i \\ \sum_{i=1}^{N^{pl}} B_i\dot{\lambda}^i \\ \sum_{i=1}^{N^{pl}} C_i\dot{\lambda}^i \end{bmatrix} \tag{26}$$

Where $\dot{\lambda}^i$ is the i-th plane plastic multiplier and $N^{pl}$ is the total number of linearization planes used. The previous constraint must hold for each point $P_i$ of each interface. Since for each point of each interface a set of $N^{pl}$ unknown plastic multipliers is defined, the total number of unknown plastic multipliers is equal to $N^{pl}\left(N_{sd}+1\right)2N_I$.

### *3.3 Non-negativity of plastic multipliers*

An additional constraint which must be included into the linear programming problem is the non-negativity of each plastic multiplier:

$$\dot{\lambda}_{ij} \geq 0. \tag{27}$$

### *3.4 Normality condition*

The last condition to be applied is the so-called normality condition which requires that the external power dissipated by the live load $\mathbf{1}\cdot\Gamma$ set equal to one, is itself equal to one, i.e.:

$$P_{\Gamma=1} = 1 \tag{28}$$

This condition allows to rewrite Eq. (12) in the following way:

$$\Gamma = \sum_{i=1}^{N_I} P_{\text{int}}^i - P_{F_0} \tag{29}$$

### 3.5 Internal dissipated power and linear programming problem

On each interface $i$, covering the surface $S_i$, the internal dissipated power is defined as the integral:

$$P_{\text{int}}^i = \int_{S_i} \boldsymbol{\sigma} \cdot \Delta\tilde{\mathbf{u}} \, dS \tag{30}$$

in the local reference system, where both $\boldsymbol{\sigma}$ and $\Delta\tilde{\mathbf{u}}$ have been defined in Subsection 3.2. Therefore, remembering Eq. (29) and following the kinematic theorem of limit analysis, the related linear programming problem can be stated as follows:

$$\min \left\{ \sum_{i=1}^{N_I} P_{\text{int}}^i - P_{\mathbf{F_0}} \right\} \tag{31}$$

under geometric constraints (15), compatibility constraints (26), non-negativity of plastic multipliers constraints (27) and the normality condition (28). The unknowns of the linear programming problem are the $6 \cdot N_E$ generalized velocity components of the center of mass of each element and the $N^{pl}\left(N_{sd}+1\right)2N_I$ plastic multipliers at each point of each interface.

## 4. GENETIC ALGORITHM

A genetic algorithm (GA) is used to adjust the mesh in order to find the minimum collapse multiplier among all possible configurations and therefore to determine the actual collapse mechanism.

A genetic algorithm is a method for solving both constrained and unconstrained optimization problems based on a natural selection process that mimics biological evolution. The algorithm repeatedly modifies a population of individual solutions. At each step, the genetic algorithm randomly selects individuals from the current population and uses them as parents to produce the children for the next generation. Over successive generations, the population "evolves" toward an optimal solution.

A NURBS mesh of a vaulted surface, is determined by a given number $N_{par}$ of real parameters

$p_1, p_2, ..., p_{Npar}$, that depend on the type of collapse mechanism which must be detected. A given NURBS mesh is regarded as an individual and each individual, is written as an array with $1 \times N_{par}$ elements:

$$individual = [p_1, p_2, ..., p_{Npar}] \tag{32}$$

Each individual has a cost, found by evaluating the cost function *f* at the parameters $p_1, p_2, ..., p_{Npar}$. The cost function *f* is defined as a function which outputs the collapse load multiplier $\lambda_c$ for every assigned individual (i.e. an assigned mesh on the surface) through the implementation of the limit analysis procedure described in Section 3:

$$\lambda_c = f(individual) = f(p_1, p_2, ..., p_{Npar}) \tag{33}$$

To begin the genetic algorithm, we define an initial population of $N_{ipop}$ individuals. In the numerical examples contained in the next Section, initial population is assumed made of 20 individuals in case of a one-parameter problem and 40 individuals in case of a three-parameter problem. A matrix represents the population with each row in the matrix being a $1 \times N_{par}$ array (individual) of continuous parameters values. Given an initial population of $N_{ipop}$ individuals, the full matrix of $N_{ipop} \times N_{par}$ random values is generated by

$$IPOP = (hi - lo) \times \mathbf{random}\{N_{ipop}, N_{par}\} + lo \tag{34}$$

where $\mathbf{random}\{N_{ipop}, N_{par}\}$ is a function that generates an $N_{ipop} \times N_{par}$ matrix of uniform random numbers, *hi* and *lo* are the highest and lowest number in the parameter range. Individuals are not all “create equal”: each one’s worth is assessed by the cost function.

In order to decide which chromosomes in the initial population of individuals are fit enough to survive and reproduce offspring in the next generation the $N_{ipop}$ costs and associated individuals are ranked from lowest cost to highest cost. We retain the best $N_{pop}$ members of the population for the next iteration of the algorithm and the rest die off. This process is called natural selection and from this point on, the size of the population at each generation is $N_{pop}$. Other and more sophisticated types of selection operators have been proposed in literature [38,39] as for instance tournament selection and proportional selection.

Then, an equal number of mothers and fathers is selected within the $N_{pop}$ individuals, which pair in some random fashion. There are various reasonable ways to pair individuals. In this paper, a weighted cost selection with assigned probabilities is used [40]. Each pair produces two offspring that contain traits from each parent. Mating is carried out by choosing one or more points in the chromosome to mark as the crossover points and the parameters between these points are merely swapped between the two parents. In this paper a multi-point crossover operator is used and $k_i = [1, 2, ..., c-1]$ crossover points are randomly selected on two individuals (parents) represented by $c$ chromosomes. Moreover, if care is not taken, the genetic algorithm may converge too quickly into one region of the cost surface and this may be not good if the problem we are modeling has several local minima, in which the solution may get trapped. To avoid this problem of overly fast convergence, we force the routine to explore other areas of the cost surface by randomly introducing changes, or mutations, in some of the parameters. A classic mutation operator is applied to all $N_{pop}$ individuals at each generation. For each individual $\mathbf{p}_i$ the mutation operator works stochastically on all the chromosomes of the individual subject to mutation (i.e. changing at random one of the individual chromosomes in the process of generating offsprings). A mutation probability of 15% has been chosen in this paper.

The algorithm described is improved by adding a zooming with elitist strategy (see e.g. [31]) in order to obtain a considerable enhancement of both robustness and efficiency of the algorithm. The zooming technique consists in sub-dividing the initial population into two groups $\bar{\mathbf{x}} = \{\bar{\mathbf{x}}_i : i = 1, ..., N_{elit}\}$ and $\mathbf{y} = \mathbf{x} - \bar{\mathbf{x}} = \{\mathbf{y}_i : i = 1, ..., N_{pop} - N_{elit}\}$ and in collecting at each iteration the individuals with higher fitness into an "elite" sub-population with user defined dimension $N_{elit}$. Afterwards, for each individual belonging to group $\bar{\mathbf{x}}$, only a mutation with high probability is applied (i.e. not crossover) in order to improve individual fitness. From a practical point of view, zooming has to be a-priori set by the user by means of the so called zooming percentage $z_{\%}$ defined as the percentage ratio between initial population size $N_{pop}$ and $\bar{\mathbf{x}}$ sub-population size $N_{elit}$. Even if zooming percentage is taken constant in this paper (equal to 5%) $z_{\%}$ can be reduced if necessary ad libitum passing from the i-th iteration to the successive one following an exponential reduction.

# 5. NUMERICAL EXAMPLES

In this Section, four numerical examples of NURBS based kinematic limit analyses of masonry vaults are described. For each example, the mid-surface of the vault has been modeled with the 3D free form modeler Rhinoceros® and the corresponding NURBS structure has been imported within a MATLAB® environment using the IGES protocol. The limit analysis procedure described in Section 3 has been implemented and the collapse mechanism is determined by suitably adjusting the mesh through the genetic algorithm described in Section 4. For each example, a number of subdivisions of the interfaces equal to $N_{sd} = 6$ is adopted.

## *5.2 Parabolic barrel vault*

In order to evaluate the applicability and reliability of the proposed kinematic limit analysis procedure for studying the behavior of masonry curved structures, a first analysis has been performed on the parabolic barrel vault belonging to Prestwood Bridge, Fig. 7.

Prestwood Bridge is a single-span masonry arch bridge located in Preston (Staffordshire, UK), and was tested up to collapse in [41], within the experimental research on masonry bridges supported by the Transport Research Laboratory (TRL). The load was applied across the bridge at quarter of the span. The configuration of the bridge just before collapse is shown in Fig. 8.

The experimental collapse load was equal to 228kN and the collapse occurred exhibiting a four hinges mechanism. The test on full-scale bridge has highlighted the strong influence of fill and spandrels on the collapse mechanisms and the load carrying capacity. For this reason, the Prestwood Bridge has become a benchmark studied by many researchers [42,43].

Following this premise, the Prestwood Bridge has been chosen as a first case study to evaluate the applicability of the proposed method to the assessment of masonry curved structures, such as the parabolic barrel vault of the bridge.

It has to be noted that the GA-NURBS analyses have been performed assuming a heavy but nonresistant fill. Consequently, the comparison with the experimental collapse mechanism may be only qualitative, because the fill is actually resistant and greatly contributes to the overall strength of the bridge.

The bridge has a net span of 6550 mm, a rise of 1428 mm and a width of 3800 mm. The vault has a span/rise ratio $R_{s/r}$ equal to about 1/5 and a curvature radius of 4.69 m and section depth is 220 mm. The ratio thickness/span $R_{t/s}$ is about 1/30 and the backfill height at the crown is 0.17 m. The geometry of the bridge is shown in Fig. 9.

**Fig. 7:** The Prestwood Bridge, Staffordshire, UK.

**Fig. 8:** Collapse of Prestwood Bridge [41].

The joints between the bricks are made of mortar. The bridge has no piers: the arch rests directly on abutments.

Following suggestions contained in [44], a masonry compression strength $f_c$ of 2.4 MPa and tensile strength $f_t$ of 0.1 MPa have been adopted, whereas a shear strength $\tau$ of 0.1 MPa is assumed. The initial NURBS mesh of the vaulted surface is composed of three quadrangular elements only. The interface between the second and the third element is fixed and is placed at quarter of net span, where a vertical point live load of $\lambda \cdot 1kN$ is applied. The interface between the first and the second element is mobile and its position is governed by the genetic algorithm. Dead loads are determined by the proper weight of masonry and infill, which is equal to $20\,kN/m^3$.

The genetic algorithm allows to evaluate the optimal position of the unloaded interface between elements, in order to minimize the collapse load multiplier and therefore obtain the actual collapse mechanism for the arch. Due to symmetry and the type of applied load, the position of this interface is defined by only one parameter. In the genetic algorithm an initial population of 10 individuals have been chosen, each individual being a scalar.

A collapse load multiplier $\lambda = 46.72$ has been obtained. Fig. 10(a) shows the 3D NURBS model of the parabolic vault generated within Rhinoceros® and Fig. 10(b) depicts the computed four-hinges collapse mechanism.

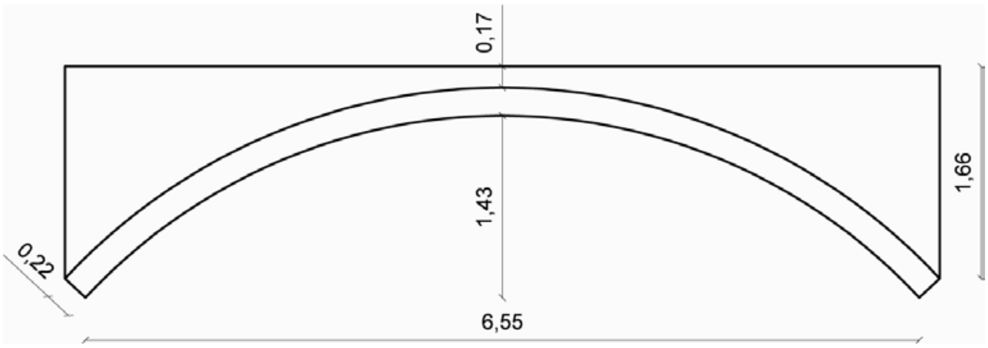


**Fig. 9:** Geometry of the Prestwood Bridge, dimensions in meters.

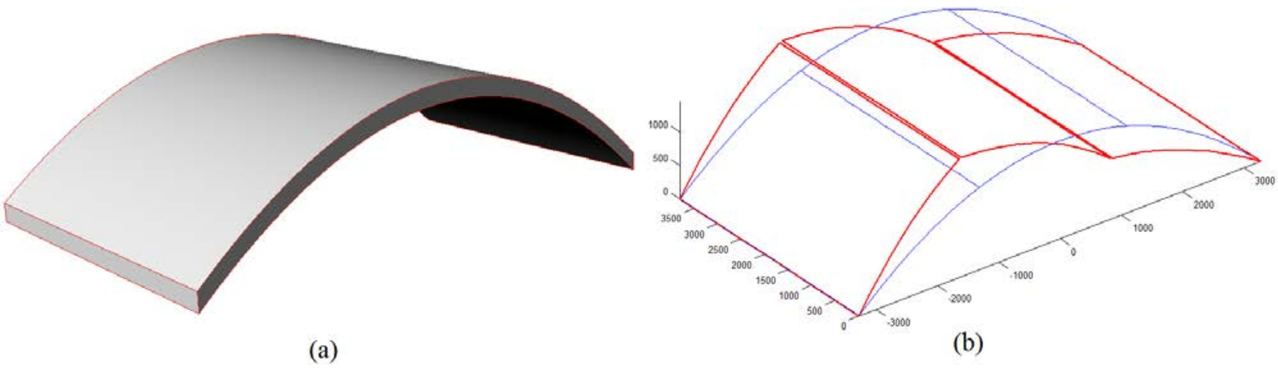


**Fig. 10:** (a) 3D NURBS model of the parabolic vault of Preston Bridge generated with Rhinoceros®. (b) Mid-surface of the three-element NURBS mesh (blue) and collapse mechanism from kinematic limit analysis (red).

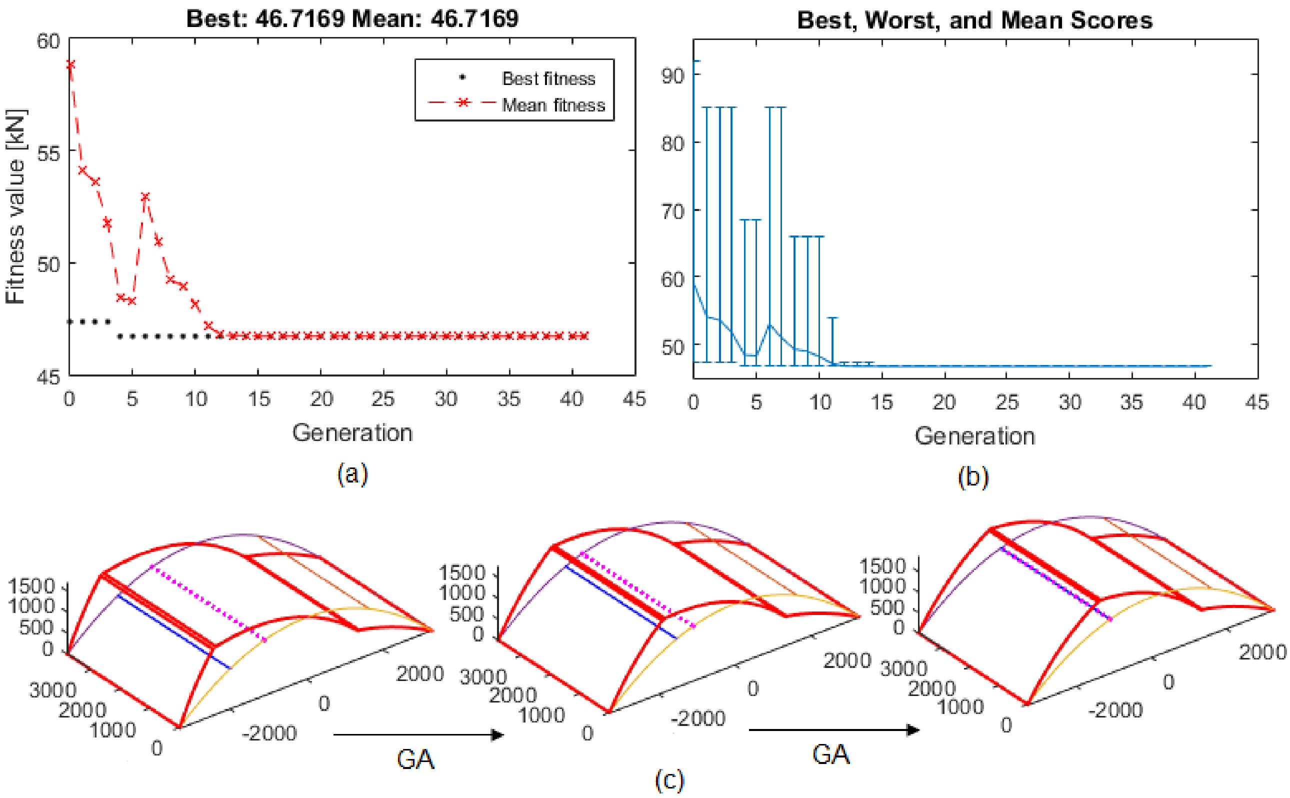


**Fig. 11:** Prestwood Bridge parabolic vault: convergence of the genetic algorithm towards the optimal solution in terms of best fitness and mean value (a) and in terms of best, worst and mean scores (b) at each generation; evolution of the free interface towards the optimal solution (c).

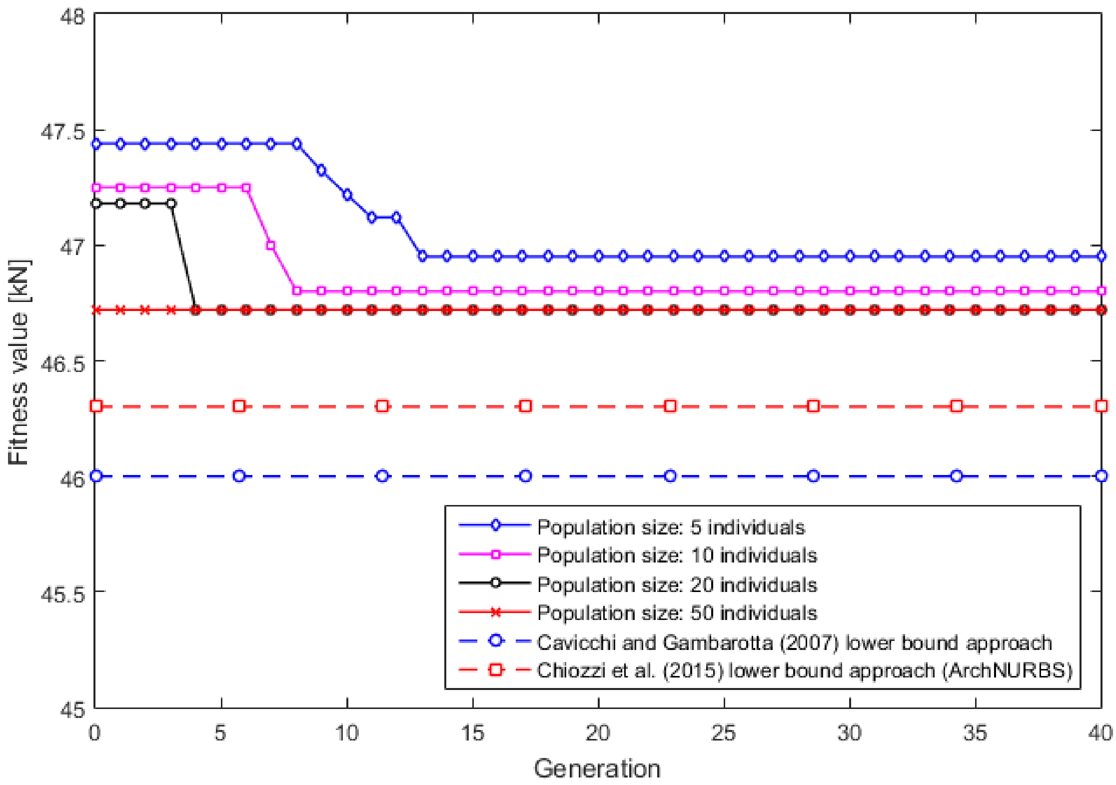


**Fig. 12:** Convergence of the proposed GA-NURBS approach for different population sizes and comparison with the lower bound approaches in [43] and [30].

As can be seen in Fig. 11(a-b), the algorithm has a fast convergence towards the optimal solution and the final best fitness value is obtained after only five generations. Fig. 11(c) represents the evolution of the mesh towards the optimal solution. The dashed interface represents the final position of the first interface, which defines the collapse mechanism.

As can be expected, the speed of convergence of the algorithm towards the optimal solution is dependent on the population size.

Nevertheless, as shown in Fig. 12, the final best fitness value can be easily obtained even with relatively small populations.

In addition, the obtained result in terms of collapse load multiplier and collapse mechanism is in agreement with both the results obtained in [43] with a finite element lower bound approach and simulations carried out with the open-source MATLAB-based code ArchNURBS developed in [30], which is devoted to the limit analysis of masonry arches and is based on a rigid-block lower bound formulation.

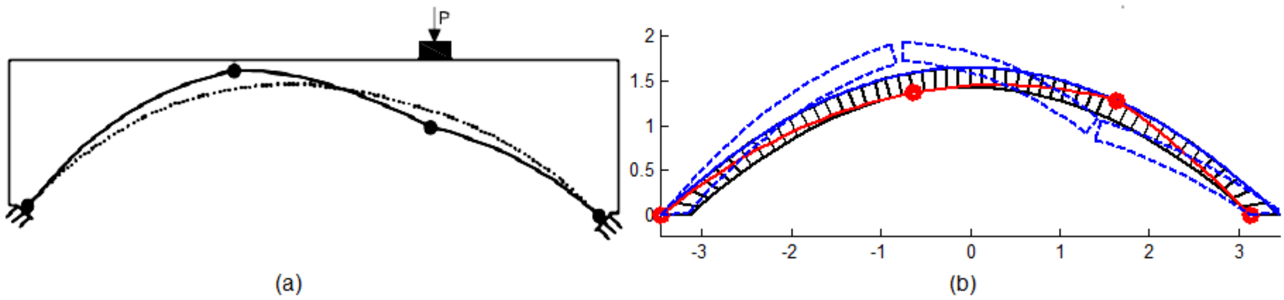


**Fig. 13:** Collapse mechanism for the Prestwood Bridge considering a heavy but nonresistant infill obtained in [43](a) and using the open-source code ArchNURBS developed in [30](b).

In particular, Fig. 13(a) represents the collapse mechanism identified in [43] for the Prestwood Bridge considering a heavy but nonresistant infill, whereas Fig. 13(b) represents the collapse mechanism computed for the same configuration using ArchNURBS.

### *5.3 Hemispherical dome*

The second analysis, heareafter discussed, concerns a hemispherical dome with an inner radius of 1150 mm and a thickness of 120 mm, which was experimentally tested in [45]. Bricks of dimensions $120 \times 250 \times 55$mm were used, with joints thickness approximately equal to 10mm. In the experiments in [45] a vertical load was applied to the upper crown and the load was increased until failure occurred. Material properties are provided in [8]: a masonry compression strength $f_c$ of 1.8 MPa and tensile strength $f_t$ of 0.1 MPa have been adopted, whereas a shear strength $\tau$ of 0.1 MPa is assumed. The initial mesh is formed by sixteen quadrangular elements obtained by fixing three parallels and eight meridians on the hemispheric NURBS surface. A vertical live load of $\lambda \cdot 1kN$ is applied at the top of the dome. Dead loads are only determined by the proper weight of masonry, assumed equal to 18 $kN/m^3$.

The genetic algorithm allows to evaluate the optimal position of the middle parallel of the mesh, in order to minimize the collapse load multiplier and therefore obtaining the actual collapse mechanism. Again, the unknown position of the mesh, due to symmetry, is governed by one parameter.

In the genetic algorithm an initial population of 10 individuals have been chosen, each individual being a scalar. A collapse load multiplier $\lambda = 52.88$ has been obtained.

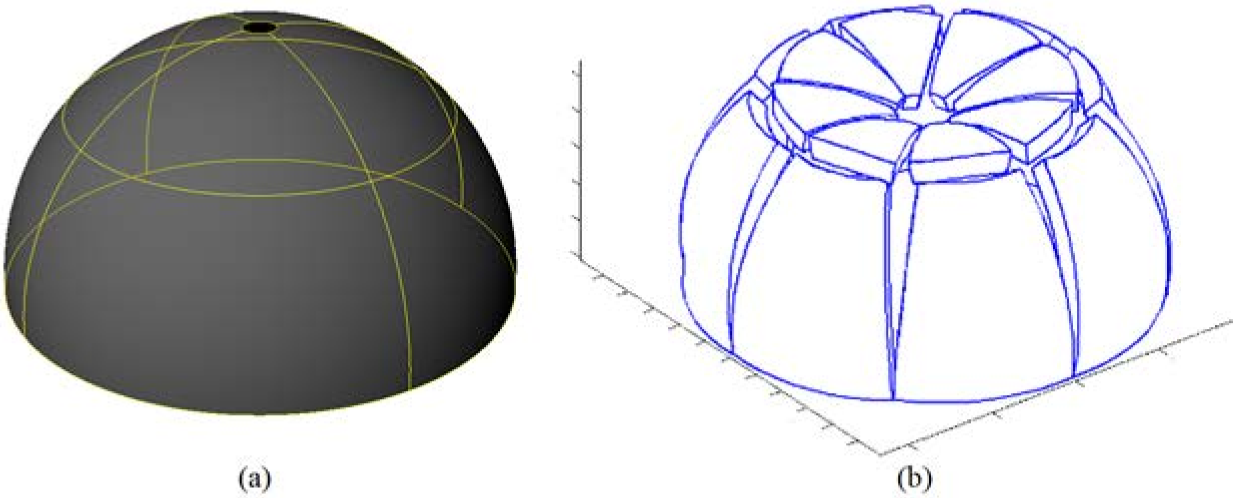

Fig. 14: (a) 3D NURBS model of the hemispherical masonry dome experimentally tested in [45] generated with Rhinoceros® and (b) 3D collapse mechanism from kinematic limit analysis for a sixteen-element NURBS mesh.

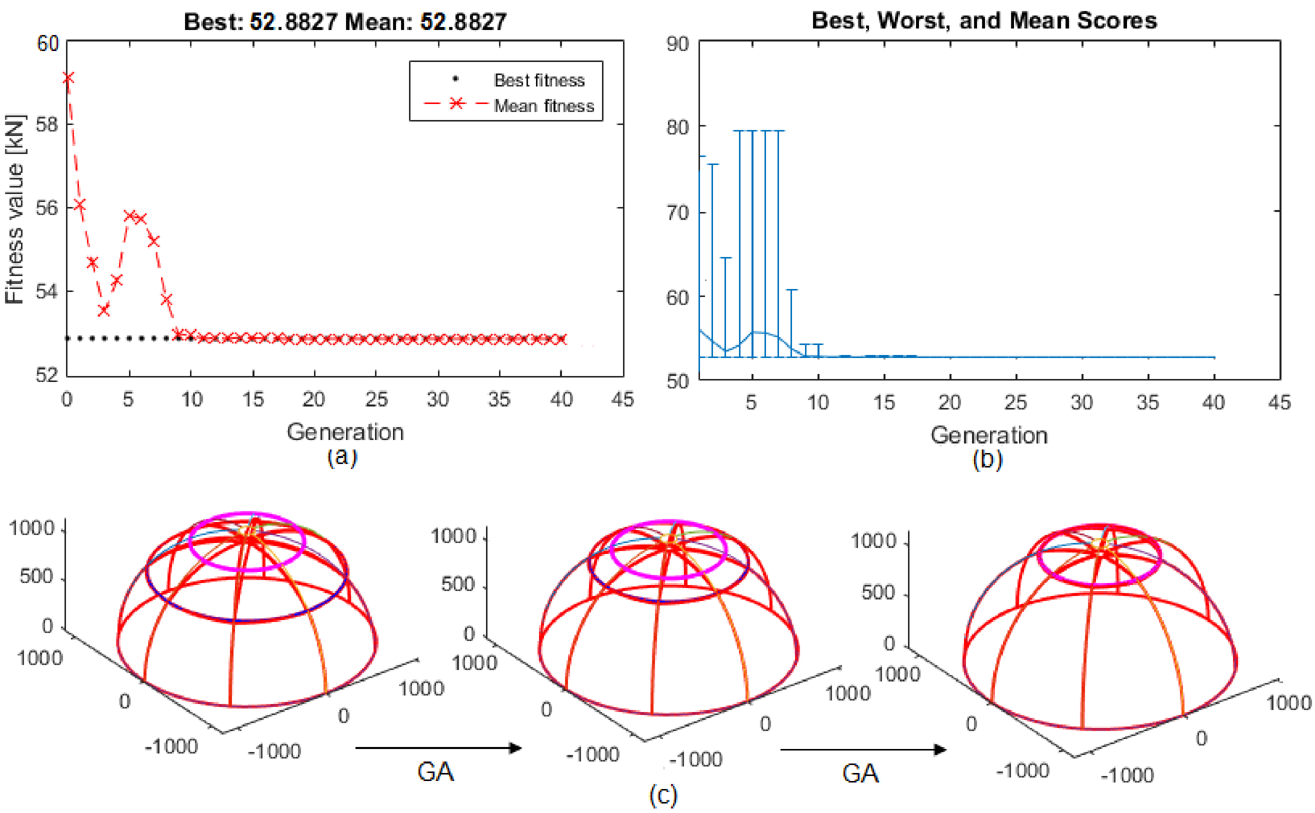


**Fig. 15:** Hemispherical dome: convergence of the genetic algorithm towards the optimal solution in terms of best fitness and mean value (a) and in terms of best, worst and mean scores (b) at each generation; evolution of the free interface towards the optimal solution (c).

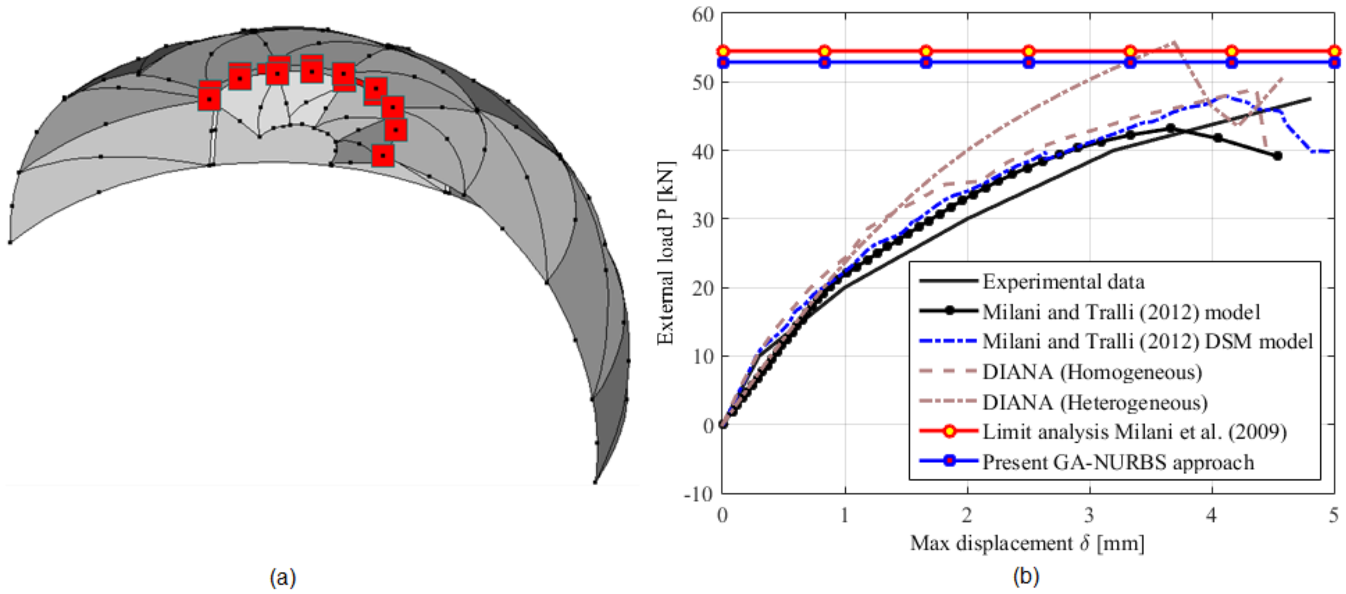


**Fig. 16:** Hemispherical dome: (a) collapse mechanism obtained with the adaptive approach described in [28]; (b) comparison between experimental results in terms of load-displacement and load-displacement response for various numerical models.

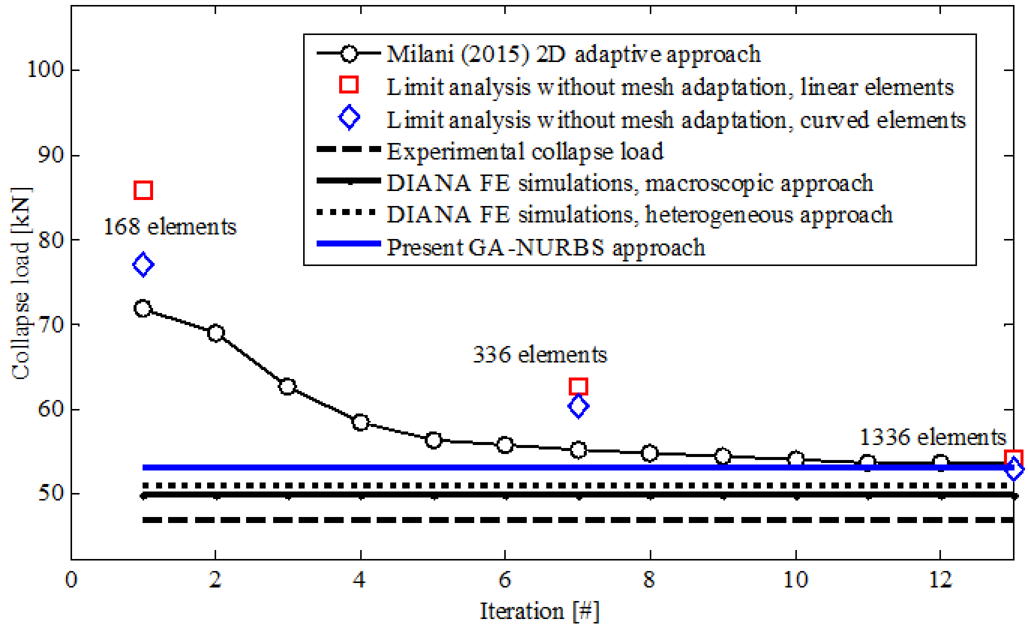


**Fig. 17:** Hemispherical dome: comparison in terms of iterations needed to catch the actual collapse load for various numerical models.

Fig. 14(a) shows the 3D NURBS model of the mid-surface of the dome generated within Rhinoceros® and Fig. 14(b) depicts the computed collapse mechanism.

As shown in Fig. 15(a-b), the algorithm presents a fast convergence towards the optimal solution and the final best fitness value is obtained since the first generation. Fig. 15(c) represents the evolution of the mesh towards the optimal solution. The dashed interface represents the final position of the first interface, which defines the collapse mechanism. Computed collapse load multiplier is very close to the one observed in [45] and later analyzed in [8] and [7].

Fig. 16(a) shows the collapse mechanism obtained with the sequential linear programming adaptive approach described in [28], which is equal to the one computed through the present GA-NURBS approach. Fig. 16(b) shows a comparison between the computed collapse load with both experimental results contained in [45] and force-displacement curves obtained through non-linear finite element analyses using the finite element software package DIANA [46], the SQP-based meso-macro model described in [7] and the limit analysis procedure proposed in [47].

It should be noted that the proposed GA-NURBS approach gives an upper bound estimate of the collapse load multiplier which is very close to the one computed in [47] and the one which can be obtained from the adaptive model described in [28].

Finally, Fig. 17 compares the number of iterations required to get the optimal solution for the [28] model and the proposed GA-NURBS approach: whereas the model in [28] requires 12 iterations, the proposed GA-NURBS approach allows for the final best fitness to be obtained after just one generation, while complete convergence of the whole population towards the best fitness value is obtained after 9 generations.

### *5.4 Skew arch*

In the third numerical simulation, the proposed GA-NURBS approach is applied to the skew circular arch experimentally tested in [48]. The arch, named *Skew 2* in [48], has a 3000mm clear square span, a 750mm rise and a skew of 45 degrees. The width of the barrel was approximately 670 mm and the average thickness 215 mm. The arch was constructed using Class A engineering bricks were on two reinforced concrete abutments representing rigid supports. The geometry of the arch is reported in Fig. 18. In the test, a concentrated load *P* was applied under force control at the three quarter span mid-width of the arch barrel. The load was monotonically increased up to 17.4kN when collapse occurred because of the formation of cracks extending in the mortar joints through the whole width of the arch, giving rise to a 3D failure mode typical of skewed masonry arches.

An average brickwork compression strength $f_c$ of 2.4 MPa and a tensile strength $f_t$ of 0.2 MPa were measured, whereas a shear strength $\tau$ of 0.1 MPa is assumed. Average specific weight of brickwork is $22\,kN/m^3$.

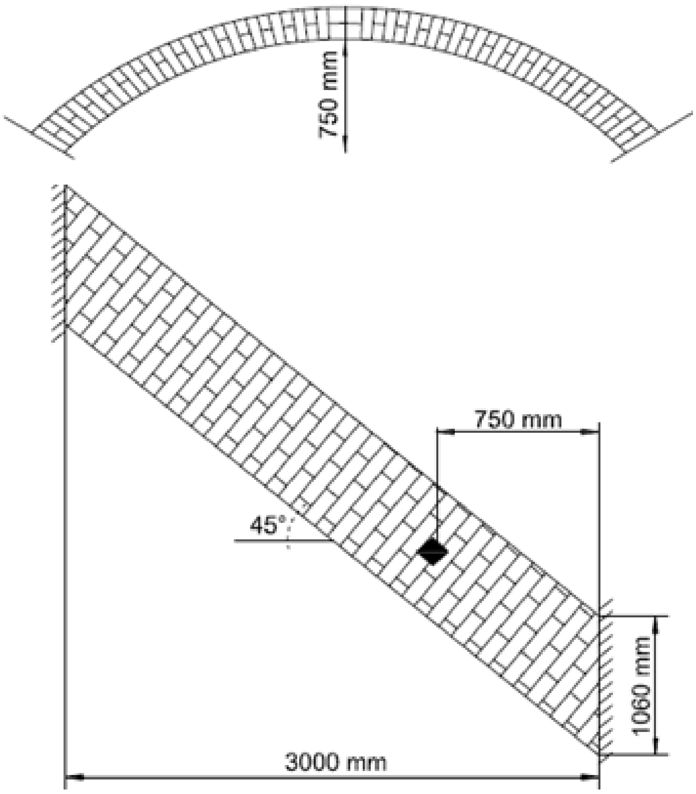


**Fig. 18:** Skew arch geometry in the test configuration described in [48].

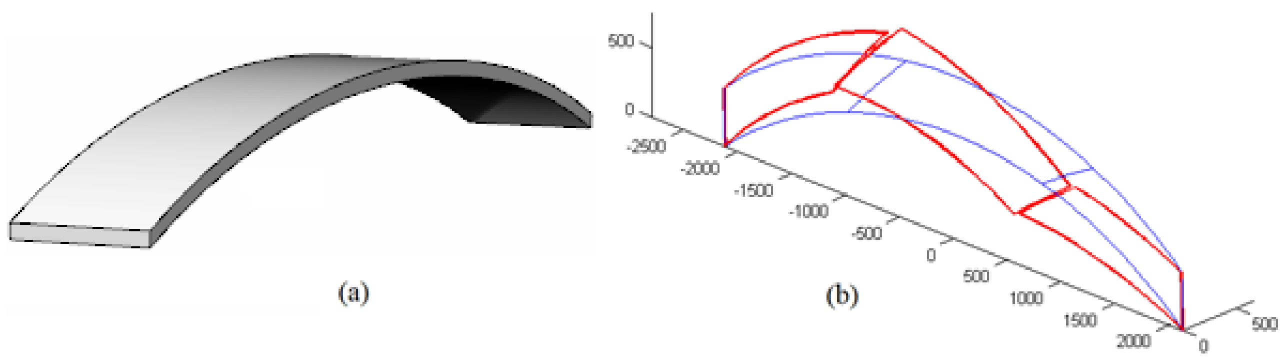


**Fig. 19**: (a) 3D NURBS model of the skew arch experimentally tested in [48] generated with Rhinoceros®. (b) Mid-surface three-element NURBS mesh (blue) and collapse mechanism from kinematic limit analysis (red).

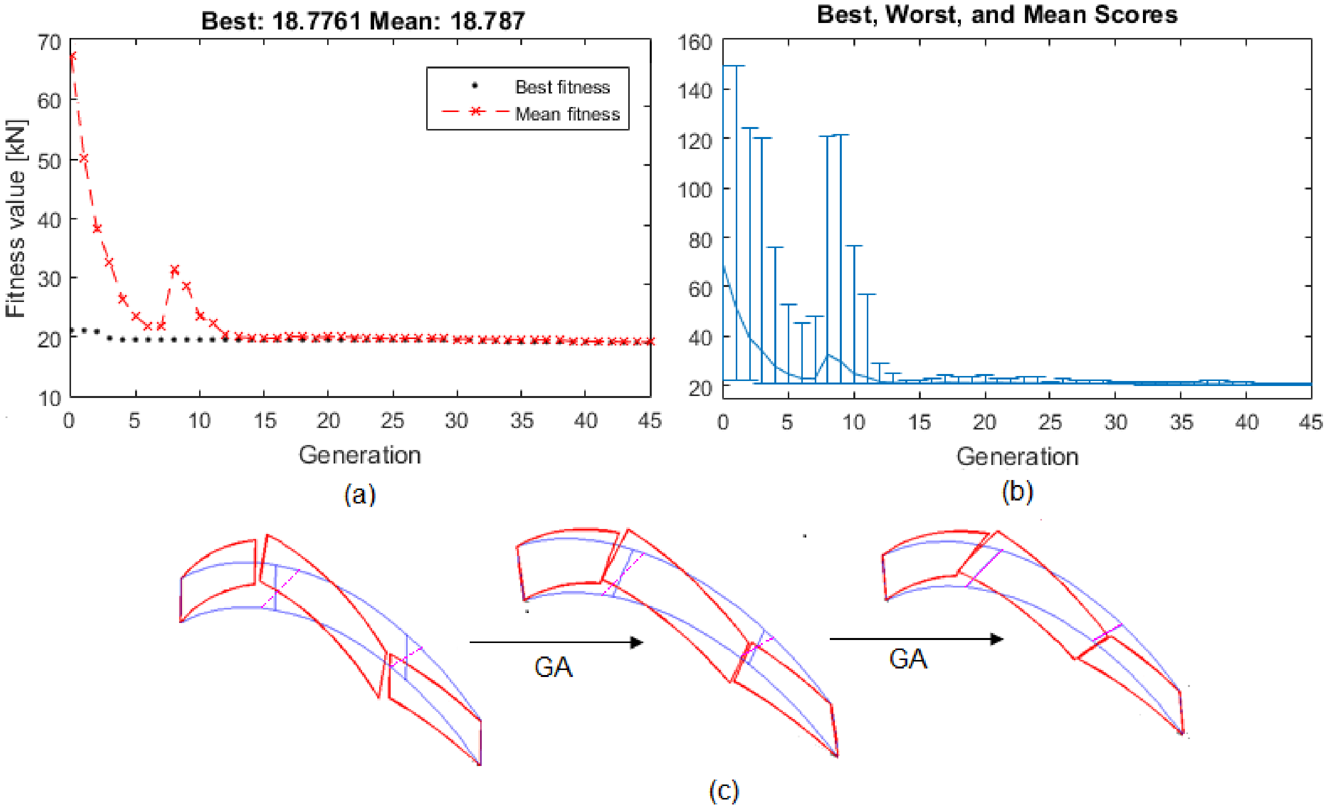


**Fig. 20:** Skew arch: convergence of the genetic algorithm towards the optimal solution in terms of best fitness and mean value (a) and in terms of best, worst and mean scores (b) at each generation; evolution of the free interfaces towards the optimal solution (c).

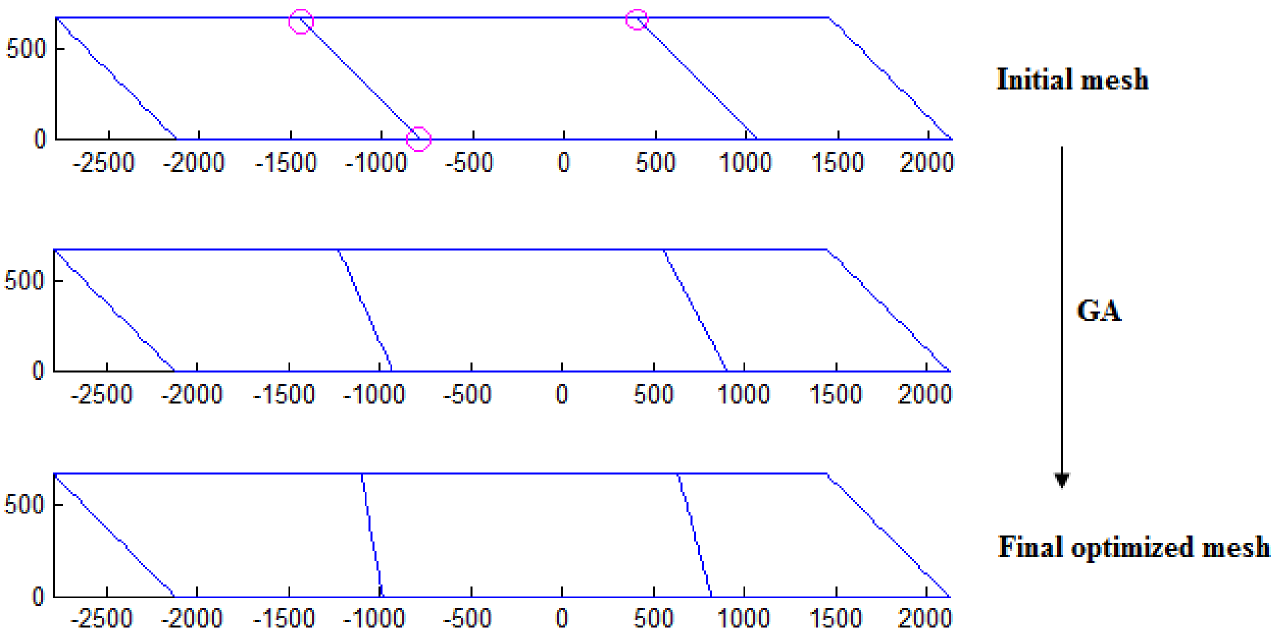


**Fig. 21:** Mesh evolution during the optimization procedure through genetic algorithm, top view. The positions of the circled vertex constitute the three parameters governing the problem.

The initial NURBS mesh of the vaulted surface is formed by three quadrangular elements. A single centered vertical live load of $\lambda \cdot 1kN$ is applied at 1/4L. The genetic algorithm allows evaluating the optimal position of the two active interfaces, in order to minimize the collapse load multiplier and therefore obtaining the actual collapse mechanism. Due to the point load presence, the position of the active interfaces is governed by three parameters: two parameters fix the extremes of the unloaded interface, whereas a third parameter fixes the position of the loaded interface (since this interface is bound to pass though the load application point).

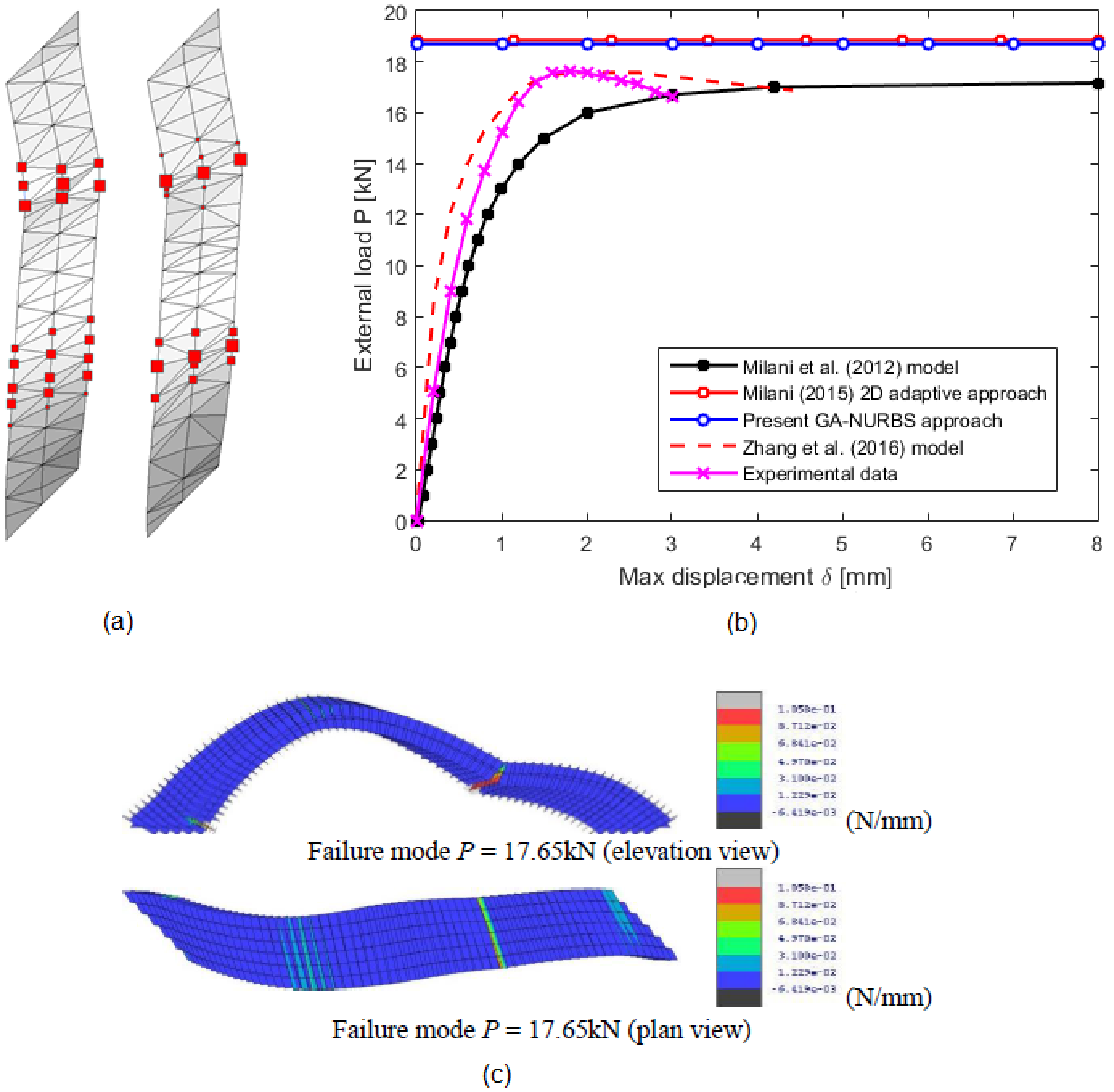


**Fig. 22:** Skew arch: (a) collapse mechanism obtained with the adaptive approach described in Milani (2015); (b) comparison between experimental data from [48], load-displacement responses predicted by various numerical models and collapse load predicted by the present GA-NURBS approach; (c) collapse mechanism obtained in [49].

In the genetic algorithm an initial population of 10 individuals have been chosen, each individual being a 1x3 vector. A collapse load multiplier $\lambda = 18.78$ has been obtained. Fig. 19(a) shows the 3D NURBS model of the vault generated within Rhinoceros® and Fig. 19(b) depicts the computed collapse mechanism, which proves to be equal to the one observed in [48].

As shown in Fig. 20(a-b), the algorithm presents a fast convergence towards the optimal solution and the final best fitness value is obtained after the first four generations. Fig. 20(c) represents the evolution of the mesh towards the optimal solution. For better visualizing the process, mesh evolution is more clearly depicted in Fig. 21. For the sake of comparison, Fig. 22(a) shows the collapse mechanism obtained with the adaptive approach described in [28], which proves to be the same as the one computed through the present GA-NURBS approach. Moreover, Fig. 22(b) shows a comparison between the computed collapse load, experimental data in [48] and the force-displacement curves obtained through the [7] model and others numerical models [28,49]. In particular, it is useful to observe that the computed collapse mechanism is in agreement with the one obtained in [49] using a mesoscale partitioned analysis, as depicted in Fig. 22(c).

### *5.5 Cross vault*

As last structural example, the cross vault experimentally tested in [50] and later analyzed in [51] is considered. The cross vault is formed by the intersection of two barrels vaults with an external radius of 2.3m and is loaded by a vertical concentrated load at the top of the extrados of one of the border arches. Bricks of dimensions $120 \times 250 \times 55$ mm$^3$ were used, with joints thickness equal to 10 mm. An average brickwork compression strength $f_c$ of 2.4 MPa and a tensile strength $f_t$ of 0.1 MPa were measured, whereas a shear strength $\tau$ of 0.1 MPa is assumed. Average specific weight of brickwork is $20\, kN/m^3$. Differently from the previous examples, the NURBS surface describing the cross vault (depicted in Fig. 24(a)) is given not by a single NURBS function, but four different NURBS patches obtained from the free form modeler used to generate the vault geometry after performing a Boolean intersection of two simple NURBS cylindrical surfaces.

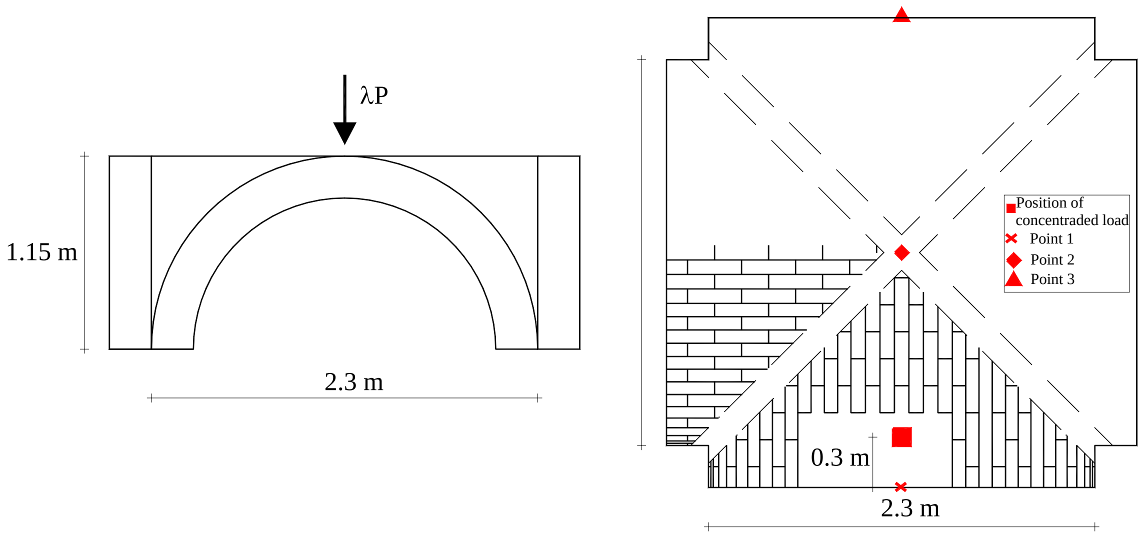


**Fig. 23:** Cross vault. Geometry and loading condition.

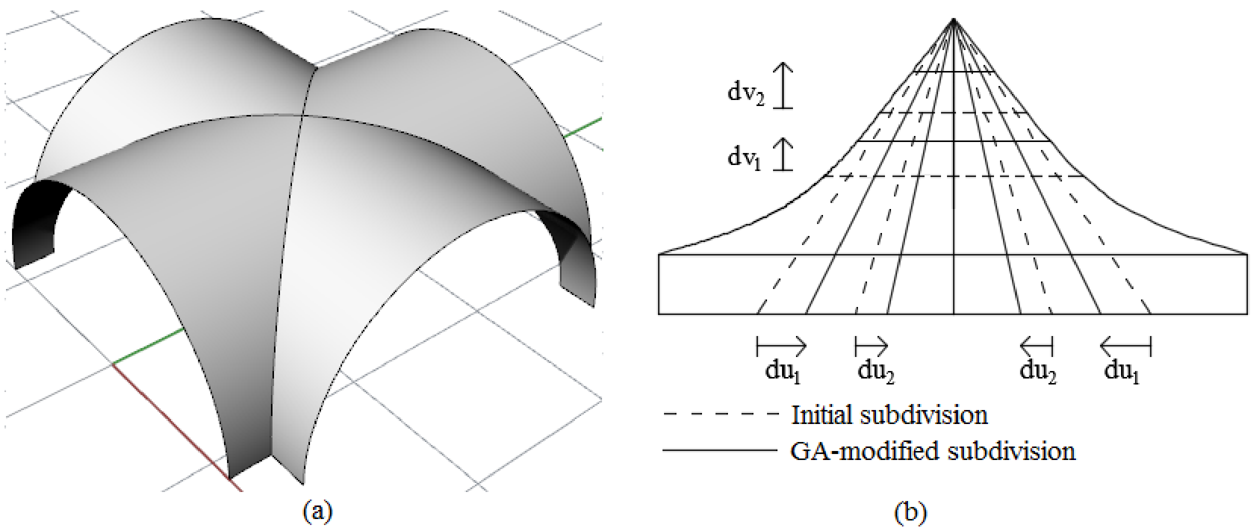


**Fig. 24:** (a) 3D NURBS model of the cross vault tested in [50] generated with Rhinoceros® and (b) NURBS parameters space and mesh parametrization.

The region of the parameter space which defines the given surface is reported in Fig. 24(b), together with the subdivision chosen for the mesh generation. In this example, the proposed subdivision and parametrization has been chosen by inspiration from classic simplified methods for the "hand" calculation of masonry vaults (see [1]). As shown in Fig. 24(b), for each patch four parameters determine the position of element interfaces. Therefore, the problem at hand is governed by twenty-four parameters. On each interface a number of $N_{sd} = 6$ subdivisions has been chosen. In the genetic algorithm an initial population of 10 individuals have been chosen, each individual being a twenty-four element vector. A collapse load multiplier $\lambda = 13.06$ has been obtained. Fig. 25(a) shows the initial undeformed 3D mesh of the cross vault whereas Fig. 25(b) depicts the computed collapse mechanism. As can be seen in Fig. 25(c-d), the algorithm has a quite fast convergence towards the optimal solution. Fig. 26(a), shows a nice agreement between the collapse load multiplier obtained through the present GA-NURBS approach and load-displacement curves obtained with the finite-element DIANA® code [46], experimental results in [50] and the failure load obtained from the homogenized limit analysis presented in [52]. Furthermore, in Fig. 26(b) the collapse mechanism obtained in [52] is reported, which again results in good agreement with the one obtained through the present GA-NURBS approach.

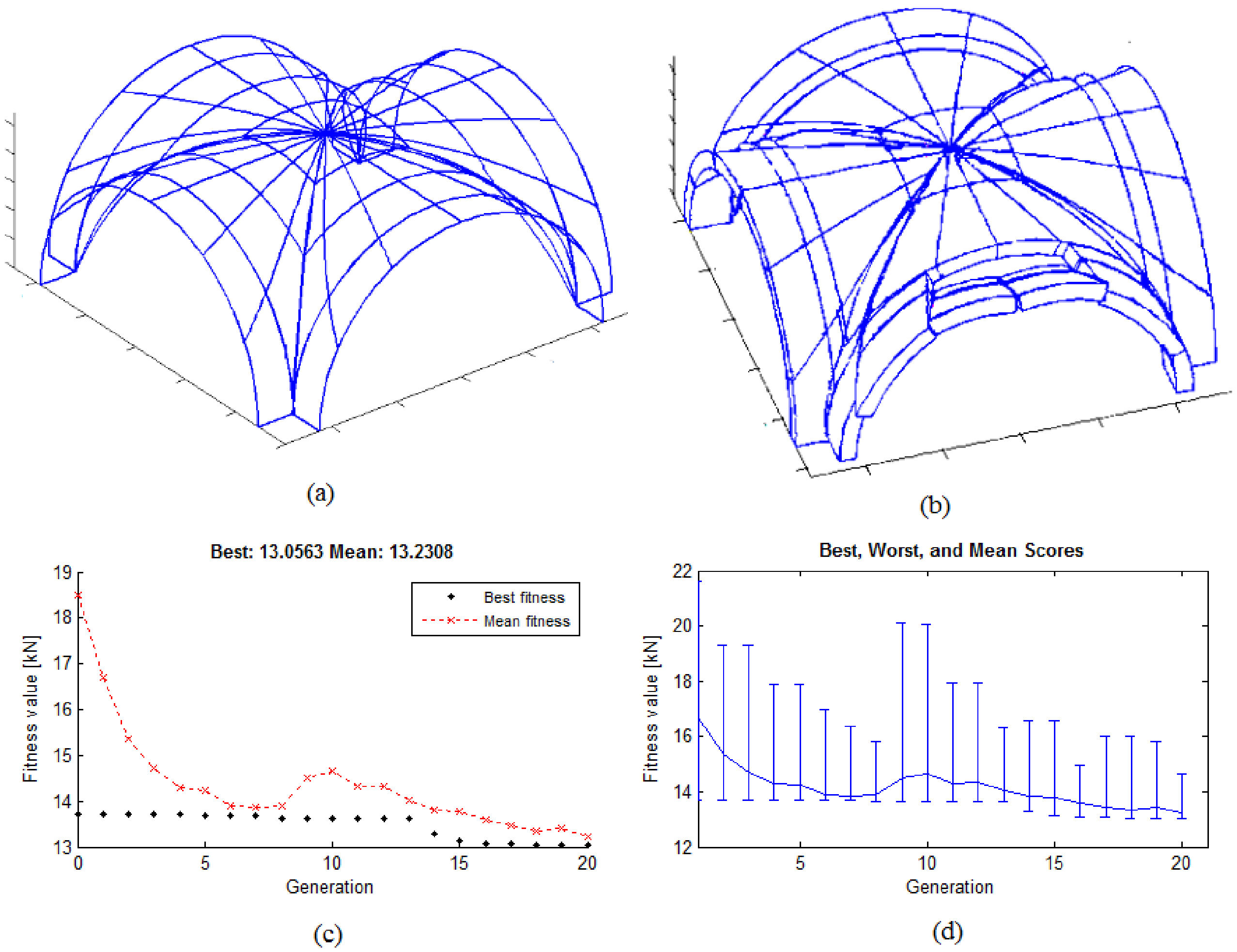


**Fig. 25:** (a) Undeformed 3D NURBS model of cross vault tested in [50]: initial mesh. (b) Collapse mechanism from kinematic limit analysis with the proposed GA-NURBS acting on a twenty-four parameter mesh. (c) Convergence of the genetic algorithm towards the optimal solution in terms of best fitness and mean value, and (d) in terms of best, worst and mean scores at each generation.

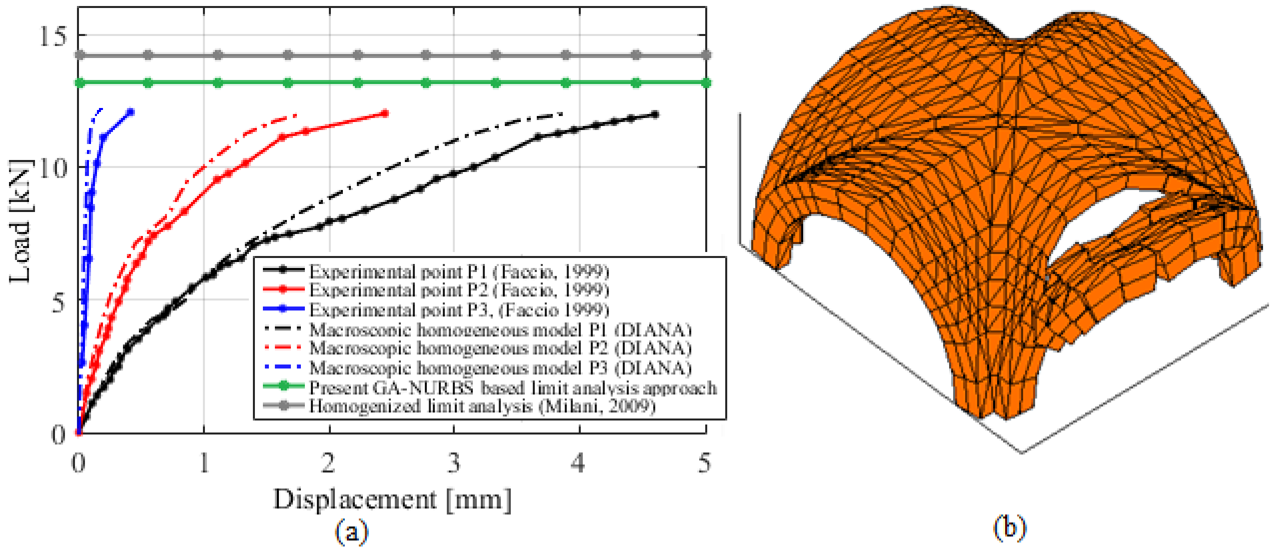


**Fig. 26:** Comparison between the results obtained with the proposed GA-NURBS and experimental results contained in [50], FEM non-linear simulations (DIANA) and homogenized limit analysis proposed in [52] in terms of collapse load multiplier (a) and failure mechanism (b).

## CONCLUSIONS

A new GA-NURBS based approach for the kinematic limit analysis of masonry vaulted structures has been presented. The main idea consists into exploiting properties of NURBS functions to develop a computationally efficient adaptive limit analysis procedure which allows to quickly evaluate the collapse load multiplier of any given masonry vault starting from its three dimensional model, which can be obtained with any free form modeler (e.g. Rhinoceros) natively working with NURBS entities. It is therefore possible to bridge the 3D modeling environment, which is very popular among professional engineers and architects, with a structural limit analysis environment in the most natural way, thus requiring the least effort to the final user and providing a high computational efficiency.

More precisely, a given reinforced masonry vault can be geometrically represented by NURBS parametric surfaces and a NURBS mesh of the given surface can be generated. Each element of the mesh is a NURBS surface itself and can be idealized as a rigid body. A homogenized upper bound limit analysis formulation, which takes into account the main characteristics of masonry material and can be deduced, with internal dissipation allowed exclusively along element edges. The approach has shown to be able to well predicting the load bearing capacity of any masonry vault of arbitrary shape, provided that the initial mesh is adaptively adjusted by means of a suitable Genetic Algorithm in order to enforce that element edges accurately approximate the actual failure mechanism. As already discussed, when analyzing masonry vaults a precise description of geometry is essential. The strength of the method lies in the fact that NURBS functions allow to discretize the original geometry by using very few elements, whose union still gives the exact geometry of the original vaulted surface. Such peculiarity allows to maximize both accuracy and computational speed. Finally, it has to be pointed out that, for most vault types, computational efficiency can be boosted by experienced users intelligently choosing a suitable mesh subdivision and parametrization, based on the knowledge of the class of failure mechanisms that the particular type of vault under study usually undergoes.

The proposed GA-NURBS approach could be further extended following different directions. In particular, future research work will include the implementation of the capability of accounting for the presence of FRP reinforcement at intrados and/or extrados, the introduction of more sophisticated backfill models, which can adequately capture soil-structure interaction effects and the implementation of an equilibrium formulation for limit analysis, which allows for a lower bound estimation of the collapse load. In fact, a lower bound estimation of the collapse load can be especially useful since it would give a precise indication of the accuracy of the solution determined through the kinematic (upper bound) formulation discussed in the present work.


## ACKNOWLEDGEMENTS

The present investigation was developed within the activities of the (Italian) University Network of Seismic Engineering Laboratories – ReLUIS, in the research program funded by the Italian Civil Protection National Service – Research Line “Masonry Structures”, WP2-WP4. A. Chiozzi and A. Tralli are grateful to Foundation Carlo Fornasini for its financial support.


## REFERENCES


[1] Como M. Statics of Historic Masonry Constructions. vol. 1. Berlin, Heidelberg: Springer Berlin Heidelberg; 2013. doi:10.1007/978-3-642-30132-2.

[2] Huerta S. The Analysis of Masonry Architecture: A Historical Approach. Archit Sci Rev 2011.

[3] Heyman J. The Stone Skeleton: Structural Engineering of Masonry Architecture. Cambridge University Press; 1997.

[4] Vasconcelos G, Lourenço PB. Assessment of the In-plane shear strength of stone masonry walls by simplified models. Proc. 5th Int. Conf. Struct. Anal. Hist. Constr., New Delhi, India: 2006.

[5] Gilbert M, Casapulla C, Ahmed HM. Limit analysis of masonry block structures with non-associative frictional joints using linear programming. Comput Struct 2006;84:873–87. doi:10.1016/j.compstruc.2006.02.005.

[6] Tralli A, Alessandri C, Milani G. Computational Methods for Masonry Vaults: A Review of Recent Results. Open Civ Eng J 2014;8.

[7] Milani G, Tralli A. A simple meso-macro model based on SQP for the non-linear analysis of masonry double curvature structures. Int J Solids Struct 2012;49:808–34. doi:10.1016/j.ijsolstr.2011.12.001.

[8] Milani E, Milani G, Tralli A. Limit analysis of masonry vaults by means of curved shell finite elements and homogenization. Int J Solids Struct 2008;45:5258–88. doi:10.1016/j.ijsolstr.2008.05.019.

[9] Block P, Ciblac T, Ochsendorf J. Real-time limit analysis of vaulted masonry buildings. Comput Struct 2006;84:1841–52. doi:10.1016/j.compstruc.2006.08.002.

[10] Block P, Lachauer L. Three-Dimensional (3D) Equilibrium Analysis of Gothic Masonry Vaults. Int J Archit Herit 2013;8:312–35. doi:10.1080/15583058.2013.826301.

[11] Angelillo M, Babilio E, Fortunato A. Singular stress fields for masonry-like vaults. Contin Mech Thermodyn 2012;25:423–41. doi:10.1007/s00161-012-0270-9.

[12] Lemos J V. Discrete Element Modeling of Masonry Structures. Int J Archit Herit 2007;1:190–213. doi:10.1080/15583050601176868.

[13] Sarhosis V, Oliveira DV, Lemos JV, Lourenco PB. The effect of skew angle on the mechanical

behaviour of masonry arches. Mech Res Commun 2014;61:53–9. doi:10.1016/j.mechrescom.2014.07.008.

[14] Sarhosis V, Bagi K, Lemos J V., Milani G. Computational Modeling of Masonry Structures Using the Discrete Element Method. IGI Global; 2016. doi:10.4018/978-1-5225-0231-9.

[15] Simon J, Bagi K. Discrete Element Analysis of the Minimum Thickness of Oval Masonry Domes. Int J Archit Herit 2016;10:457–75. doi:10.1080/15583058.2014.996921.

[16] Chetouane B, Dubois F, Vinches M, Bohatier C. NSCD discrete element method for modelling masonry structures. Int J Numer Methods Eng 2005;64:65–94. doi:10.1002/nme.1358.

[17] Rafiee A, Vinches M, Bohatier C. Application of the NSCD method to analyse the dynamic behaviour of stone arched structures. Int J Solids Struct 2008;45:6269–83. doi:10.1016/j.ijsolstr.2008.07.034.

[18] Hazay M, Munjiza A, Baraldi D, Reccia E, Cazzani A, Cecchi A, et al. Introduction to the Combined Finite-Discrete Element Method. Comput. Model. Mason. Struct. Using Discret. Elem. Method, vol. 4, IGI Global; 1AD, p. 123–45. doi:10.4018/978-1-5225-0231-9.ch006.

[19] Reccia E, Cecchi A, Milani G, Alpa G, Monetto I, Anthoine A, et al. FEM/DEM Approach for the Analysis of Masonry Arch Bridges. Comput. Model. Mason. Struct. Using Discret. Elem. Method, vol. 42, IGI Global; 1AD, p. 367–92. doi:10.4018/978-1-5225-0231-9.ch014.

[20] Sloan SW, Kleeman PW. Upper bound limit analysis using discontinuous velocity fields. Comput Methods Appl Mech Eng 1995;127:293–314. doi:10.1016/0045-7825(95)00868-1.

[21] Yu X, Tin-Loi F. A simple mixed finite element for static limit analysis. Comput Struct 2006;84:1906–17. doi:10.1016/j.compstruc.2006.08.019.

[22] Chen S, Liu Y, Cen Z. Lower bound shakedown analysis by using the element free Galerkin method and non-linear programming. Comput Methods Appl Mech Eng 2008;197:3911–21. doi:10.1016/j.cma.2008.03.009.

[23] Tin-Loi F, Ngo NS. Performance of the p-version finite element method for limit analysis. Int J Mech Sci 2003;45:1149–66. doi:10.1016/j.ijmecsci.2003.08.004.

[24] Ngo NS, Tin-Loi F. Shakedown analysis using the -adaptive finite element method and linear programming. Eng Struct 2007;29:46–56. doi:10.1016/j.engstruct.2006.03.033.

[25] Lyamin AV, Krabbenhøft K, Sloan SW, Hjiaj M. An adaptive algorithm for upper bound limit analysis using discontinuous velocity fields. Proc. Eur. Congr. Comput. Methods Appl. Sci. Eng. (ECCOMAS 2004), Jyväskylä, Finland: 2004.

[26] Lyamin A V., Sloan SW, Krabbenhøft K, Hjiaj M. Lower bound limit analysis with adaptive remeshing. Int J Numer Methods Eng 2005;63:1961–74. doi:10.1002/nme.1352.

[27] Milani G, Lourenço PB. A discontinuous quasi-upper bound limit analysis approach with sequential linear programming mesh adaptation. Int J Mech Sci 2009;51:89–104. doi:10.1016/j.ijmecsci.2008.10.010.

[28] Milani G. Upper bound sequential linear programming mesh adaptation scheme for collapse analysis of masonry vaults. Adv Eng Softw 2015;79:91–110. doi:10.1016/j.advengsoft.2014.09.004.

[29] Piegl L, Tiller W. The NURBS Book. Berlin, Heidelberg: Springer Berlin Heidelberg; 1995. doi:10.1007/978-3-642-97385-7.

[30] Chiozzi A, Malagù M, Tralli A, Cazzani A. ArchNURBS: NURBS-Based Tool for the Structural Safety Assessment of Masonry Arches in MATLAB. J Comput Civ Eng 2015.

[31] Milani G, Milani F. Genetic algorithm for the optimization of rubber insulated high voltage power cables production lines. Comput Chem Eng 2008;32:3198–212. doi:10.1016/j.compchemeng.2008.05.010.

[32] Cottrell JA, Hughes TJR, Bazilevs Y. Isogeometric Analysis: Toward Integration of CAD and FEA. John Wiley & Sons; 2009.

[33] McNeel R. Rhinoceros: Nurbs Modeling for Windows. Robert McNeel & Associates; 2008.

[34] USPRO. Initial Graphics Exchange Specification, IGES 5.3. U.S. Product Data Association; 1996.

[35] Aboudi J. Mechanics of Composite Materials: A Unified Micromechanical Approach.

Elsevier; 2013.

[36] Taliercio A. Closed-form expressions for the macroscopic in-plane elastic and creep coefficients of brick masonry. Int J Solids Struct 2014;51:2949–63. doi:10.1016/j.ijsolstr.2014.04.019.

[37] Milani G, Taliercio A. In-plane failure surfaces for masonry with joints of finite thickness estimated by a Method of Cells-type approach. Comput Struct 2015;150:34–51. doi:10.1016/j.compstruc.2014.12.007.

[38] Goldberg DE. Genetic Algorithms in Search, Optimization, and Machine Learning. Addison-Weasley Publishing Company; 1989.

[39] Kwon Y-D, Kwon S-B, Jin S-B, Kim J-Y. Convergence enhanced genetic algorithm with successive zooming method for solving continuous optimization problems. Comput Struct 2003;81:1715–25. doi:10.1016/S0045-7949(03)00183-4.

[40] Haupt RL, Haupt SE. Practical Genetic Algorithms. John Wiley & Sons; 2004.

[41] Page J. Load Tests to Collapse on Two Arch Bridges at Preston, Shropshire and Prestwood, Staffordshire. TRRL Res Rep 1987.

[42] Cavicchi A, Gambarotta L. Two-dimensional finite element upper bound limit analysis of masonry bridges. Comput Struct 2006;84:2316–28. doi:10.1016/j.compstruc.2006.08.048.

[43] Cavicchi A, Gambarotta L. Lower bound limit analysis of masonry bridges including arch–fill interaction. Eng Struct 2007;29:3002–14. doi:10.1016/j.engstruct.2007.01.028.

[44] CIRC2009. Instructions for the Application of the New Italian Building Code D.M. 14/01/2008 (in Italian). G.U. n. 47 26/02/2009; 2009.

[45] Foraboschi P. Masonry structures externally reinforced with FRP strips: tests at collapse. Proc. 1st Convegno Naz. “Sperimentazioni su Mater. e Strutt., Venice, Italy: 2006.

[46] TNO DIANA. DIANA Finite Element Software Package 2015.

[47] Milani G, Milani E, Tralli A. Upper Bound limit analysis model for FRP-reinforced masonry curved structures. Part I: Unreinforced masonry failure surfaces. Comput Struct

2009;87:1516–33. doi:10.1016/j.compstruc.2009.07.007.
[48] Wang J, Melbourne C. The 3-Dimensional Behaviour of Skew Masonry Arches. London, UK: 1996.
[49] Zhang Y, Macorini M, Izzudin BA. Mesoscale Partitioned Analysis of Brick-Masonry Arches. Eng Struct 2016;to appear.
[50] Faccio P, Foraboschi P, Siviero E. Masonry vaults reinforced with FRP strips (in italian). L'Edilizia 1999;7-8:44–50.
[51] Creazza G, Matteazzi R, Saetta A, Vitaliani R. Analyses of Masonry Vaults: A Macro Approach based on Three-Dimensional Damage Model. J Struct Eng 2002;128:646–54. doi:10.1061/(ASCE)0733-9445(2002)128:5(646).
[52] Milani G, Milani E, Tralli A. Upper bound limit analysis model for FRP–reinforced masonry curved structures. Part II: Structural analyses. Comput Struct 2009;87:1534–58. doi:10.1016/j.compstruc.2009.07.010.